The suitability of different swirl number definitions for describing swirl flows: Accurate, common and (over-) simplified formulations

Guillaume Vignat, D. Durox, Sébastien Candel

The suitability of different swirl number definitions for describing swirl flows: accurate, common and (over-) simplified formulations

Guillaume Vignat[a,*], Daniel Durox[a], Sébastien Candel[a]

[a]*Laboratoire EM2C, CNRS, CentraleSupélec, Université Paris-Saclay, 3, rue Joliot Curie, 91190 Gif-sur-Yvette, France*

Abstract

Swirling flows are of considerable practical importance. They are used for example to increase heat transfer in pipes or to stabilize flames at a distance from the injector unit by means of a central reverse flow that establishes an inner recirculation zone of hot combustion products. The level of swirl is governed by a dimensionless parameter designated as the swirl number, which essentially quantifies the ratio of the flow rate of the angular momentum axial component to the flow rate of axial momentum. This ratio controls to a great extent the structure of the swirling flow and its value determines whether an inner recirculation zone is established and whether a precessing vortex core (PVC) is formed in the flow. However, a major difficulty resides in calculating the swirl number from experimental measurements and over the last 50 years, several simplified formulas have been proposed to overcome this difficulty. The present study is aimed at using velocity and pressure profiles obtained by a large eddy simulation in a generic configuration to examine these simplified expressions and determine the conditions under which they may be applicable. The geometry comprises a cylindrical swirling injector, flush mounted in the back plane of a cylindrical cavity. Although the swirl number is in principle constant when the flow is established in a duct with a constant cross-section, provided that viscous forces at the wall are negligible, one finds that this quantity varies substantially if inadequate approximations are made. Among the many possibilities one concludes that two swirl numbers should be distinguished. The first corresponding to the original definition features conservation properties, but is difficult to properly calculate from experimental data. The second is a highly simplified formulation that is commonly used today but does not share the conservation properties of the first formulation. Recommended practices are provided on how each of these swirl numbers should be calculated. It is also shown that the other formulations yield values that notably differ from those provided by the original definition.

Keywords:
Swirling flow; Swirl number; Large Eddy Simulation

Contents

*Corresponding author:
Email address: guillaume.vignat@centralesupelec.fr (Guillaume Vignat)

Abbreviations

AMR	Adaptive Mesh Refinement	NSCBC	Navier-Stokes Characteristic Boundary Conditions
AVBP	LES Navier-Stokes solver	ORZ	Outer Recirculation Zone
BL	Boundary layer	PIV	Particle Image Velocimetry
IRZ	Internal Recirculation Zone	PVC	Precessing Vortex Core
LDV	Laser Doppler Velocimetry	RMS	Root Mean Square
LES	Large Eddy Simulation	TTGC	Two-step Taylor Galerkin numerical scheme
LIKE	Loss in Kinetic Energy		

Roman symbols

A_t	Total cross-section of tangential channels
D_{sw}	Swirler outlet diameter
D_{ch}	Tangential channel diameter
D_Q	Diameter of combustor cavity
e_r, e_θ, e_x	Radial, tangential and axial directions
G_θ	Axial component of flow rate of angular momentum
G_x	Flow rate of axial momentum
L_Q	Combustion chamber length
L_{inj}	Injector length
M	Flow momentum (Boussinesq) coefficient
$\dot{m}$	Mass flow rate
$\dot{m}_{nom}$	Nominal mass flow rate
$\dot{m}_{rec}$	Recirculating mass flow rate in a given section
p	Pressure
p_∞	Pressure at an infinite radial position
p_{atm}	Atmospheric pressure
p_{ref}	Reference pressure
r	Radial coordinate
R	Reference radius
R_c	Radius of cylindrical cavity
R_{inj}	Radius of injector outlet
R_{lim}	Radial integration upper limit
R_0	Distance between tangential channels and swirler axis
Re	Reynolds number
Ro	Rossby number
S	Swirl number
S_{conv}	Conventional swirl number
S_{geo}	Swirl number geometrical formulation
U	Sectional mean of axial velocity
U_r, U_θ, U_x	Radial, tangential and axial velocity components
u_r, u_θ, u_x	Radial, tangential and axial velocity fluctuations
x	Axial coordinate

Subscripts and superscripts applicable to S, G_x and G_θ

^{f}	Fluctuation terms are included	$_0$	Pressure term neglected
^{0}	Fluctuation terms are neglected	$_U$	Pressure term estimated in terms of velocity
$_P$	Pressure term is included	$_{U,BL}$	Pressure term estimated using boundary layer approx.

1. Introduction

Swirling flows are widely used in practice [1], whether to favor mixing [2–5], to increase heat transfer in ducted flows [6, 7] or to stabilize flames in combustors [8–16]. These flows can alter their behaviour entirely as a function of the swirl level. It is known that swirl notably impacts pollutant emissions, determines the flame dynamics [13, 14, 16**? ? ?** –18] and that processes like blow out and flashback can be controlled by suitably distributing swirl [12**? ?**]. Multi-swirl arrangements like the double annular staged combustor (DAC) or the twin annular premixing swirler (TAPS) have been designed to control combustion. Early investigations indicated that it was worth defining a dimensionless group to classify swirling flows and determine critical values corresponding to various flow regimes. The Rossby number defined as the ratio of the mean axial velocity $< \overline{U}_x >$ to the azimuthal flow velocity ΩR

$$\mathrm{Ro} = \frac{< \overline{U}_x >}{\Omega R} \tag{1}$$

is commonly employed to analyze flows rotating at a rate Ω and featuring a typical scale R. The vortex breakdown phenomenon taking place in such flows was generally characterized in terms of this dimensionless number [19–22]. This was adequate because in the relatively low Reynolds number flows that were investigated ($\mathrm{Re} < 10^3$), a solid body rotation could be assumed so that the Rossby number could be easily determined. In higher Reynolds number flows like those generated by combustor injectors, which are the main focus of the present article, the Rossby number is difficult to define in a precise manner because the flow is non uniform. This was noticed in some early studies on swirling injectors and a dimensionless group that had a greater degree of generality was proposed by Rose [23] and Chigier and his coworkers [9, 24–26]. The swirl number concept was widely adopted as it essentially compares flow rates of quantities of interest obtained by integration across an axial cross-section at a position x

$$S(x) = \frac{1}{R(x)} \frac{G_\theta(x)}{G_x(x)} \tag{2}$$

where G_θ is the time average of the flow rate of the angular momentum axial component integrated over the axial cross-section, R is a characteristic radius of the swirling flow and G_x is the time average of the flow rate of axial momentum across the axial cross-section [1]. Independently of these early works, Reynolds [28] showed using a similarity analysis that the swirl number is the controlling parameter in the decay of swirling wakes and jets. As will be seen later, G_θ and G_x are conserved in free jets and in confined flows if the duct has a constant cross-section and viscous losses at the wall are negligible. These conservation properties enhance the degree of generality of the dimensionless number defined by Eq. (2) and this expression may be used with some confidence to characterize rotating flows. In axisymmetric configurations these fluxes may be written as follows [1, 23–25]

$$G_\theta = 2\pi \int_0^\infty \rho r^2 \left(\overline{U_\theta}\,\overline{U_x} + \overline{u_\theta u_x}\right) dr \tag{4}$$

$$G_x = 2\pi \int_0^\infty r \left[(\overline{p} - p_\infty) + \rho(\overline{U_x}^2 + \overline{u_x^2})\right] dr \tag{5}$$

In the previous expressions $\overline{U}$ and u respectively designate mean and fluctuating velocity components. As G_θ and G_x are conserved, at least in certain types of flows, this is translated into a constant swirl number [24], a feature that is crucial for its accurate determination from measured velocity profiles. In practice however, the previously defined G_x and G_θ are replaced by simplified formulations but it is not easy to say if this does not reduce the degree of generality that was initially sought in defining the swirl number. The objective of the present work is to compare the various formulations and extract expressions that are most representative and are best suited to characterize flows formed by injectors in combustion systems.

The motivation of this investigation lies on the idea that flows which have the same swirl number and the same Reynolds number will also have similar dynamics. It is known for example that above a critical swirl number, vortex breakdown takes place and a recirculation zone is formed [19, 21, 22, 29–31]. For swirled jets at a high Reynolds numbers, vortex breakdown is manifested by a bubble-type recirculation region located on the axis of the injector [**?**] designated as the Central Recirculation Zone (CRZ). In flows inside tubes of constant section it is possible to observe other types of vortex breakdown configurations [1, 21, 22, 32], giving rise to spiral structures. The bubble-type vortex breakdown is often associated with another hydrodynamic instability, the Precessing Vortex Core (PVC) which is characterized by one or more helical vortex structures rotating around the recirculation zone [1, 22, 24, 30, 33, 34]. When it appears, the PVC extends axially over a distance of one to two diameters from the injector outlet. The frequency of PVC linearly depends on the injector flow rate [**? ?**]. When there is only one helical structure around the CRZ, it is no longer perfectly axisymmetric. It is deformed by the cyclic passage of the PVC around it [19**?**]. When the PVC is present, it creates a strong interaction with the central recirculation zone. Turbulence is locally

[1] As noted by Yajnik and Subbaiah [27], the swirl number is related to the Rossby number with the following velocity U^* and rotation rate Ω^* scales:

$$\mathrm{Ro} = \frac{U^*}{\Omega^* R},\ G_\theta = \pi\rho U^* \Omega^* R^4,\ G_x = \pi\rho U^{*2} R^2 \tag{3}$$

augmented and transport is intensified. In particular in combustion, the presence of a PVC will help stabilize the flame, by accelerating mixing [33**?** **?**]. But the PVC is not always present when vortex breakdown takes place. It can be present under non-reactive conditions but disappears when a flame is established [34–36]. When there is a thermoacoustic instability in a swirled flame burner its influence is often reduced [37], it can also be present during part of the instability cycle and disappear during the opposite phase [**?**].
It is difficult to precisely define a swirl number that constitutes a threshold for vortex breakdown. If a value of 0.6 is often cited [**?**] many other values are quoted : 0.48 [38], or 0.45 [39], or 0.94 as in [40]. This obviously depends on how the swirl number is determined but some further studies indicate that the flow dynamics depends not only on the swirl number but also on the initial conditions [38, 41]. Escudier and Keller [42] and Altgeld [43] further demonstrate that the outlet boundary conditions influence the near-field dynamics of subcritical non-reactive swirling flows, a result also observed in reactive conditions in [44, 45]. The work of Weber and Dugue [12] additionally suggests that in reactive flows, the strength of the inner recirculation zone can be estimated based on a swirl number accounting for the increase in temperature.

In practice, the variability of these results can be to some extent attributed to the different simplified formulations adopted to calculate the swirl number. It is thus worth re-examining the simplified swirl number formulations for isothermal flows. An unusual choice is made of augmenting the literature review by a validated LES, which is used to test and examine the different swirl number formulations compare the corresponding expressions, obtain estimates and analyze their behavior as the flow evolves in the axial direction. It is believed that this is more complete than a pure literature review would be on its own.

This article is organized as follows. The next section contains a brief review of the different swirl number formulations derived from the Reynolds-averaged Navier-Stokes equations. This section includes the various combinations that may be deduced from the original definition and an expression that is most commonly used in practice that may be designated as "conventional". The computational geometry introduced in section 3 corresponds to a generic experimental configuration that is later used to validate the numerical simulations. The numerical set up is also briefly described in section 3. Experimental data are compared to the simulation results, and the general structure of the flow is examined in section 4. The various simplified formulations of the swirl number, and the axial evolution thereof, are then compared in section 5. Section 6 specifically discusses a conventional swirl number formulation that is commonly employed in the literature. A few appendices are concerned with various practical aspects and some complementary analysis. Appendices A and B present recommended procedures that may be used in the practical computation of the swirl number from experimental or simulation data. Appendix C is concerned with the comparison of the flow and resulting swirl number obtained in a confined and unconfined configuration. The jump condition at a sudden expansion is discussed in Appendix D.

2. A brief review of swirl number derivations and corresponding expressions

2.1. Free swirling jets

Formulations for the swirl number depend on the simplifications introduced to estimate the integrated fluxes defined previously. The method for writing the swirl number in terms of velocities and static pressure is described in [25] and more recently in [5]. The main steps are briefly reviewed to underline the main points in the most common simplifications.

Chigier and Chervinsky [25] employ the integral techniques used in shear flow theory. A similar process is used in what follows. It is convenient to begin with the Navier-Stokes equations for an axisymmetric, stationary, incompressible, newtonian flow. The Reynolds-averaged Navier-Stokes equations expressed in a cylindrical set of coordinates write

$$\frac{1}{r}\frac{\partial(r\overline{U_r})}{\partial r} + \frac{\partial\overline{U_x}}{\partial x} = 0 \tag{6}$$

$$\overline{U_r}\frac{\partial \overline{U_r}}{\partial r} + \overline{U_x}\frac{\partial \overline{U_r}}{\partial x} - \frac{\overline{U_\theta}^2}{r} = -\frac{1}{\rho}\frac{\partial \overline{p}}{\partial r} - \left[\frac{\partial \overline{{u_r}^2}}{\partial r} + \frac{\partial \overline{u_r u_x}}{\partial x} + \frac{1}{r}\left(\overline{{u_r}^2} - \overline{{u_\theta}^2}\right)\right] + \frac{1}{\rho}\left[\frac{1}{r}\frac{\partial r\overline{\tau_{rr}}}{\partial r} + \frac{\partial \overline{\tau_{rx}}}{\partial x} - \frac{1}{r}\overline{\tau_{\theta\theta}}\right] \tag{7}$$

$$\overline{U_r}\frac{\partial \overline{U_\theta}}{\partial r} + \overline{U_x}\frac{\partial \overline{U_\theta}}{\partial x} + \frac{\overline{U_r}\,\overline{U_\theta}}{r} = -\left[\frac{\partial \overline{u_\theta u_x}}{\partial x} + \frac{1}{r^2}\frac{\partial (r^2\overline{u_r u_\theta})}{\partial r}\right] + \frac{1}{\rho}\left[\frac{1}{r^2}\frac{\partial r^2\overline{\tau_{\theta r}}}{\partial r} + \frac{\partial \overline{\tau_{\theta x}}}{\partial x}\right] \tag{8}$$

$$\overline{U_r}\frac{\partial \overline{U_x}}{\partial r} + \overline{U_x}\frac{\partial \overline{U_x}}{\partial x} = -\frac{1}{\rho}\frac{\partial \overline{p}}{\partial x} - \left[\frac{\partial \overline{u_x^2}}{\partial x} + \frac{1}{r}\frac{\partial (r\overline{u_r u_x})}{\partial r}\right] + \frac{1}{\rho}\left[\frac{1}{r}\frac{\partial r\overline{\tau_{rx}}}{\partial r} + \frac{\partial \overline{\tau_{xx}}}{\partial x}\right] \tag{9}$$

where the mean and fluctuating velocity components satisfy the following boundary conditions

$$\begin{aligned}
\overline{U_x}(x, r=\infty) = u_x(t, x, r=\infty) = 0 \\
\overline{U_r}(x, r=0) = \overline{U_r}(r=\infty) = u_r(t, x, r=\infty) = 0 \\
\overline{U_\theta}(x, r=0) = \overline{U_\theta}(x, r=\infty) = u_\theta(t, x, r=\infty) = 0 \\
\frac{\partial \overline{U_\theta}}{\partial r}(x, r=0) = \frac{\partial \overline{U_\theta}}{\partial r}(x, r=\infty) = 0 \\
\overline{\tau}(x, r=\infty) = \underline{\underline{0}}
\end{aligned} \tag{10}$$

The balance for the flow rate of axial momentum G_x can be obtained by first multiplying Eq. (9) by r and integrating between $r = 0$ and $r = \infty$. Using Eq. (6), this yields

$$\frac{d}{dx}\int_0^\infty r\left[(\overline{p} - p_\infty) + \rho(\overline{U_x}^2 + \overline{u_x^2})\right]dr = \frac{d}{dx}\int_0^\infty r\overline{\tau_{xx}}dr \tag{11}$$

The viscous term appearing in the right hand side is usually neglected as swirling flows of interest are generally characterized by a high Reynolds number. The pressure at $r = \infty$, p_∞, is included in this expression in order for the integral to remain finite. This is specific to free swirling jet flows. Equation (11) then expresses the conservation of G_x:

$$\frac{dG_x}{dx} = \frac{dG^f_{x,P}}{dx} = 2\pi\frac{d}{dx}\int_0^\infty r\left[(\overline{p} - p_\infty) + \rho(\overline{U_x}^2 + \overline{u_x^2})\right]dr = 0 \tag{12}$$

The notation $G^f_{x,P}$ is introduced to indicate that G_x comprises the fluctuating (superscript f) and pressure (subscript P) terms, which are often neglected due to the difficulty involved in the determination of pressure inside the flow [1, 10].

A convenient formulation removing the need for pressure measurements is derived in [25]. The Navier-Stokes equations, Eqs. (6) - (9), are first simplified by considering that in a swirling jet, viscous terms can be neglected and boundary layer assumptions can be adopted. For more details on the use of boundary layer assumptions in shear flows, see for example Pope [46]. Equation (7) simplifies into

$$-\frac{\overline{U_\theta}^2}{r} = -\frac{1}{\rho}\frac{\partial \overline{p}}{\partial r} - \left[\frac{\partial \overline{{u_r}^2}}{\partial r} + \frac{1}{r}\left(\overline{{u_r}^2} - \overline{{u_\theta}^2}\right)\right] \tag{13}$$

Multiplying Eq. (13) by r^2 and integrating the result between $r = 0$ and $r = \infty$ yields

$$\int_0^\infty r\,(\overline{p} - p_\infty)\,dr = -\frac{1}{2}\int_0^\infty \rho r\,(\overline{U_\theta}^2 + \overline{u_r^2} + \overline{u_\theta^2})\,dr \tag{14}$$

This result is sometimes combined with a simplified form of Eq. (13) where fluctuations are neglected [25, 47]. One may then write

$$\frac{\partial \overline{p}}{\partial r} \simeq \rho \frac{\overline{U_\theta}^2}{r} \tag{15}$$

Equations (14) and (11) can be merged into

$$\frac{d}{dx}\int_0^\infty \rho r \left(\overline{U_x}^2 - \frac{\overline{U_\theta}^2}{2} + \overline{u_x^2} - \frac{\overline{u_r^2} + \overline{u_\theta^2}}{2} \right) dr = 0 \tag{16}$$

To get a simplified version it is sometimes assumed that $\overline{u_x^2} - (\overline{u_r^2} + \overline{u_\theta^2})/2$ is negligible with respect to U_x^2 to obtain

$$\frac{d}{dx}\int_0^\infty \rho r \left(\overline{U_x}^2 - \frac{\overline{U_\theta}^2}{2} \right) dr = 0 \tag{17}$$

This last result (17) is used for example by Ribeiro and Whitelaw [2] to define a simplified expression of G_x, that can be called $G^0_{x,U,BL}$, where the superscript 0 indicates that velocity fluctuations are neglected, and the subscript U, BL that a velocity expression is used to replace the pressure term under a boundary layer assumption:

$$G^0_{x,U,BL} = 2\pi \int_0^\infty \rho r \left(\overline{U_x}^2 - \frac{\overline{U_\theta}^2}{2} \right) dr \tag{18}$$

In distinction with Chigier and Chervinsky [25], Örlü and Alfredsson [5] keep the fluctuating terms in their final result and express the conservation of the flow rate of axial momentum in the form

$$G^f_{x,U,BL} = 2\pi \int_0^\infty \rho r \left(\overline{U_x}^2 - \frac{\overline{U_\theta}^2}{2} + \overline{u_x^2} - \frac{\overline{u_r^2} + \overline{u_\theta^2}}{2} \right) dr \tag{19}$$

The simplified expressions (18) and (19) account for effects of static pressure within the swirling flow without direct measurements of the corresponding term. These expressions however assume a high Reynolds number and use an approximation of the radial pressure gradient in terms of the mean azimuthal velocity.

Consider now the axial axial component of the flow rate of angular momentum G_θ defined as

$$G_\theta = G^f_\theta = 2\pi \int_0^\infty \rho r^2 \left(\overline{U_\theta}\,\overline{U_x} + \overline{u_\theta u_x} \right) dr \tag{20}$$

Here again, the superscript f indicates that the fluctuations are kept in G^f_θ. By multiplying Eq. (8) by r^2 and integrating between 0 and ∞, the following expression can be obtained for the balance of the flow rate of the angular momentum axial component

$$\frac{d}{dx}\int_0^\infty \rho r^2 \left(\overline{U_\theta}\,\overline{U_x} + \overline{u_x u_\theta} \right) dr = \frac{d}{dx}\int_0^\infty r^2\, \overline{\tau_{\theta x}}\, dr \tag{21}$$

As for Eq. (11), the viscous term in the right hand side is generally neglected. Keeping the fluctuating term, Örlü and Alfredsson [5] obtain the following expression

$$\frac{d}{dx}\int_0^\infty r^2 \left(\overline{U_\theta}\,\overline{U_x} + \overline{u_\theta u_x} \right) dr = 0 \tag{22}$$

When the cross-correlation of the fluctuating velocities is neglected [25], the previous expression simplifies to

$$\frac{d}{dx}\int_0^\infty r^2\, \overline{U_\theta}\,\overline{U_x}\, dr = 0 \tag{23}$$

Equations (11), (16) and (17) correspond to conservation relations for G_x under various simplifying assumptions and similarly, Eqs. (22) and (23) to conservation relations for G_θ. These results may then be combined in various ways to yield a set of expressions for the swirl number defined by Eq. (2). In the remainder of the paper, the swirl number will be notated as S_{sub}^{super}. The superscript f is used to indicate that the fluctuating terms $\overline{u_\theta u_x}$ and $\overline{u_x^2}$ are kept, while the superscript 0 indicates that they are neglected. The subscript P is used to indicate that the pressure term $\overline{p} - p_\infty$ is kept, while the subscript 0 indicates that it is neglected, and the subscript U, BL that $\overline{p} - p_\infty$ is replaced with the velocity formulation introduced in Eq. (19). The same notation is used for simplified formulations for the integrated fluxes G_x and G_θ.

The most complete formulation for the swirl number S_P^f takes into account both the static pressure term and the velocity fluctuations. The reference radius R used in the swirl number definition for free jets (Eq. (2)) is the injector radius at its oulet.

$$S_P^f = \frac{G_\theta^f}{RG_{x,P}^f} = \frac{\int_0^\infty \rho\,(\overline{U_\theta}\,\overline{U_x} + \overline{u_\theta u_x})\,r^2 dr}{R\int_0^\infty \left[(\overline{p} - p_\infty) + \rho\,(\overline{U_x}^2 + \overline{u_x^2})\right] r dr} \tag{24}$$

If the turbulent fluctuations terms are deleted one has

$$S_P^0 = \frac{G_\theta^0}{RG_{x,P}^0} = \frac{\int_0^\infty \rho\,\overline{U_\theta}\,\overline{U_x}\,r^2 dr}{R\int_0^\infty \left[(\overline{p} - p_\infty) + \rho\,\overline{U_x}^2\right] r dr} \tag{25}$$

Since static pressure and density are difficult to measure inside the flow, their variations are often neglected in the expression of the swirl number and the following expression is widely used

$$S_0^0 = \frac{G_\theta^0}{RG_{x,0}^0} = \frac{\int_0^\infty \rho\,\overline{U_\theta}\,\overline{U_x}\,r^2 dr}{R\int_0^\infty \rho\,\overline{U_x}^2 r dr} \tag{26}$$

To get closer to the original formulation S_P^f, but to avoid measuring the static pressure, it is possible to write the conservation of the axial flow rate of axial momentum expressed in terms of velocities only (Eq. (16)). Under boundary layer assumptions, the expression of the swirl number then takes the form

$$S_{U,BL}^f = \frac{G_\theta^f}{RG_{x,U,BL}^f} = \frac{\int_0^\infty \rho\,(\overline{U_\theta}\,\overline{U_x} + \overline{u_\theta u_x})\,r^2 dr}{R\int_0^\infty \rho\left(\overline{U_x}^2 - \frac{1}{2}\overline{U_\theta}^2 + \overline{u_x^2} - \frac{1}{2}(\overline{u_r^2} + \overline{u_\theta^2})\right) r dr} \tag{27}$$

If the fluctuation terms are neglected, this becomes

$$S_{U,BL}^0 = \frac{G_\theta^0}{RG_{x,U,BL}^0} = \frac{\int_0^\infty \rho\,\overline{U_\theta}\,\overline{U_x}\,r^2 dr}{R\int_0^\infty \rho\left(\overline{U_x}^2 - \frac{1}{2}\overline{U_\theta}^2\right) r dr} \tag{28}$$

A new swirl number formulation is introduced in the present article (section 5.3). Similarly to $S_{U,BL}^f$, it expresses the conservation of the axial flow rate of axial momentum in terms of velocities only, but it does no rely on a boundary layer simplification. It writes

$$S_U^f = \frac{G_\theta^f}{RG_{x,U}^f} = \frac{\int_0^\infty \rho\left(\overline{U_\theta}\,\overline{U_x} + \overline{u_\theta u_x}\right) r^2 dr}{R\int_0^\infty \rho\left[\overline{U_x}^2 + \overline{u_x^2} - \frac{1}{2}\left(\overline{U_\theta}^2 + \overline{U_r}^2 + \overline{u_r^2} + \overline{u_\theta^2}\right) + \frac{r}{2}\frac{\partial}{\partial x}\left(\overline{U_x}\,\overline{U_r} + \overline{u_x u_r}\right)\right] r dr} \tag{29}$$

These six formulations use different levels of simplification, and the aim of this article is to examine the impact of these simplifications on the calculated swirl numbers. It is also natural to add to these formulations an expression that will be designated as "conventional"

$$S_{conv} = \frac{\int_0^{R_{lim}} \rho\,\overline{U_\theta}\,\overline{U_x}\,r^2 dr}{R\int_0^{R_{lim}} \rho\,\overline{U_x}^2 r dr} \tag{30}$$

The reference radius R is taken equal to the injector radius while the radial limit of integration R_{lim} needs to be specified on physical grounds. We will see that this may be defined by considering the radial evolutions of the flow rates $G^0_{x,0}$ and G^0_θ.

2.2. Confined flows

In the previous developments all integrations are carried out from 0 to ∞, but it is evident that these integrations stop at a place where the jet velocity has essentially vanished, or at a radial distance R_c if the flow is confined by a duct of radius R_c.

It is thus logical to examine swirling flows confined in a duct of constant radius R_c. A no-slip boundary condition is used at the duct wall and Eq. (10) is then

$$\begin{aligned} \overline{U_x}(x, r = R_c) = u_x(t, x, r = R_c) = 0 \\ \overline{U_r}(x, r = 0) = \overline{U_r}(r = R_c) = u_r(t, x, r = R_c) = 0 \\ \overline{U_\theta}(x, r = 0) = \overline{U_\theta}(x, r = R_c) = u_\theta(t, x, r = R_c) = 0 \end{aligned} \tag{31}$$

The definition of G_x is then

$$G_x = G^f_{x,P} = 2\pi \int_0^{R_c} r\left[(\overline{p} - p_{ref}) + \rho(\overline{U_x}^2 + \overline{u_x^2})\right] dr \tag{32}$$

and Eq. (11) writes

$$\frac{dG^f_{x,P}}{dx} = 2\pi \frac{d}{dx}\left(\int_0^{R_c} r\overline{\tau_{xx}} dr\right) + 2\pi R_c \, \overline{\tau_{rx}}|_{r=R_c} \tag{33}$$

A reference pressure is not strictly required but is included to keep formulations similar to those derived for free swirling jets allowing direct comparisons between confined and unconfined cases. Furthermore, the pressure term $\overline{p} - p_{ref}$ then has the same order of magnitude as that of the velocity term $\rho(\overline{U_x}^2 + \overline{u_x^2})$, a feature of practical interest. There is no widespread consensus on the choice of the reference value p_{ref}. It is often suggested that it may be taken equal to a pressure at the wall as this yields relatively simple expressions for the swirl number [12, 47]. This point will be considered in subsection 5.2. One should note that the expression put forward by Weber and Dugué [12] contains a mistake, which was identified and corrected by Zhao and Weber [48], thus recovering the same expression as [47]. The right hand side term in Eq. (33) comprises viscous terms, accounting for dissipation in the flow and at the wall. Mattingly and Oates [47] derived the following balance while neglecting the turbulent fluctuating terms and working under a high Reynolds number assumption except at the wall

$$\frac{d}{dx}\int_0^{R_c} r\left[(\overline{p} - p_{ref}) + \rho\overline{U_x}^2\right] dr = R_c \, \overline{\tau_{rx}}|_{r=R_c} \tag{34}$$

Here, the right hand side is the axial component of the wall shear stress. Using the method of [25], Mattingly and Oates propose an equation similar to Eq. (14) for confined flows

$$\int_0^{R_c} r\,(\overline{p} - p_{ref})\, dr = \frac{1}{2}R_c^2(\overline{p}|_{r=R_c} - p_{ref}) - \frac{\rho}{2}\int_0^{R_c} r\,(\overline{U_\theta}^2 + \overline{u_r^2} + \overline{u_\theta^2})\, dr \tag{35}$$

This leads to the following balance equation for the flow rate of axial momentum

$$G_x = G^f_{x,U,BL} = 2\pi \int_0^{R_c} r\rho\left[\overline{U_x}^2 - \frac{1}{2}\overline{U_\theta}^2 + \overline{u_x}^2 - \frac{1}{2}\left(\overline{u_r}^2 + \overline{u_\theta}^2\right)\right] dr + \pi R_c^2(\overline{p}|_{r=R_c} - p_{ref}) \tag{36}$$

$$\frac{dG^f_{x,U,BL}}{dx} = 2\pi R_c \, \overline{\tau_{rx}}|_{r=R_c} \tag{37}$$

The axial flow rate of moment of angular momentum is defined as

$$G_\theta = G^f_\theta = 2\pi \int_0^{R_c} \rho r^2 \left(\overline{U_\theta}\,\overline{U_x} + \overline{u_r u_\theta}\right) dr \tag{38}$$

and its changes in the axial direction may be deduced from the momentum balance equation (Eq. (8))

$$\frac{dG_\theta^f}{dx} = 2\pi \frac{d}{dx}\int_0^{R_c} \rho r^2 \left(\overline{U_\theta}\,\overline{U_x} + \overline{u_r u_\theta}\right) dr = 2\pi \frac{d}{dx}\left(\int_0^{R_c} r^2\,\overline{\tau_{\theta x}}\,dr\right) + 2\pi R_c^2\,\overline{\tau_{r\theta}}|_{r=R_c} \tag{39}$$

The viscous losses in the flow are neglected by most authors. Mattingly and Oates [47] however keep the wall shear stress term $R_c^2\,\overline{\tau_{r\theta}}|_{r=R_c}$. Equations (24) to (29) can then be adapted to confined flows in ducts with a radius R_c which now constitutes the upper limit of integration.

$$S_P^f = \frac{G_\theta^f}{R_c G_{x,P}^f} = \frac{\int_0^{R_c} \rho\,(\overline{U_\theta}\,\overline{U_x} + \overline{u_\theta u_x})\,r^2 dr}{R_c \int_0^{R_c}\left[(\overline{p} - p_{ref}) + \rho\,(\overline{U_x}^2 + \overline{u_x^2})\right] r dr} \tag{40}$$

$$S_P^0 = \frac{G_\theta^0}{R_c G_{x,P}^0} = \frac{\int_0^{R_c} \rho\,\overline{U_\theta}\,\overline{U_x}\,r^2 dr}{R_c \int_0^{R_c}\left[(\overline{p} - p_{ref}) + \rho\,\overline{U_x}^2\right] r dr} \tag{41}$$

$$S_0^0 = \frac{G_\theta^0}{R_c G_{x,0}^0} = \frac{\int_0^{R_c} \rho\,\overline{U_\theta}\,\overline{U_x}\,r^2 dr}{R_c \int_0^{R_c} \rho\,\overline{U_x}^2 r dr} \tag{42}$$

$$S_{U,BL}^f = \frac{G_\theta^f}{R_c G_{x,U,BL}^f} = \frac{\int_0^{R_c} \rho\,(\overline{U_\theta}\,\overline{U_x} + \overline{u_\theta u_x})\,r^2 dr}{R_c[\int_0^{R_c} \rho\left(\overline{U_x}^2 - \frac{1}{2}\overline{U_\theta}^2 + \overline{u_x^2} - \frac{1}{2}(\overline{u_r^2} + \overline{u_\theta^2})\right) r dr + \frac{1}{2}{R_c}^2\left(\overline{p}|_{r=R_c} - p_{ref}\right)]} \tag{43}$$

$$S_U^f = \frac{\int_0^{R_c} \rho\left(\overline{U_\theta}\,\overline{U_x} + \overline{u_\theta u_x}\right) r^2 dr}{R_c \int_0^{R_c} \rho\left[\overline{U_x}^2 + \overline{u_x^2} - \frac{1}{2}\left(\overline{U_\theta}^2 + \overline{U_r}^2 + \overline{u_r^2} + \overline{u_\theta^2}\right) + \frac{r}{2}\frac{\partial}{\partial x}\left(\overline{U_x}\,\overline{U_r} + \overline{u_x u_r}\right)\right] r dr + \frac{R_c^3}{2}\left(\overline{p}|_{r=R_c} - p_{ref}\right)} \tag{44}$$

One may note that many authors employing Eq. (43) use a reference pressure equal to the pressure at the wall in the axial section where the swirl number is measured, thereby eliminating the term $\frac{1}{2}R_c^2\left(\overline{p}|_{r=R_c} - p_{ref}\right)$ [3, 12, 47, 49]. The reference pressure then varies with the axial position in the system. This assumption together with the suppression of the turbulent terms yields a fairly simple expression

$$S_{U,BL}^0 = \frac{G_\theta^0}{R_c G_{x,u}^0} = \frac{\int_0^{R_c} \rho\,\overline{U_\theta}\,\overline{U_x}\,r^2 dr}{R_c \int_0^{R_c} \rho\left(\overline{U_x}^2 - \frac{1}{2}\overline{U_\theta}^2\right) r dr} \tag{45}$$

Finally, it is worth noting that the conservation properties that have been demonstrated here for G_θ^f, $G_{x,P}^f$ and the swirl number S_P^f in a cylindrical duct extend to all confinements with a constant cross-section as shown in appendix **??**.

2.3. Geometrical formulations

The previous expressions require measurements of velocity profiles that are not always available. They are often replaced by algebraic expressions based on the injector geometry. The present section focuses on expressions suited for the geometry presented in Fig. 1, where a radial swirler is placed at the bottom of a cylindrical injection duct. Some assumptions are always placed on the shape for the velocity profiles, which may not necessarily be realistic. One such expression for the swirl number of radial swirlers fed by tangential channels only involves the swirler outlet diameter D_{sw}, the radial distance R_0 separating the axis of each tangential channel from the injector axis and A_t the total cross-section area of these channels [50, 51]

$$S_{geo,1} = \frac{\pi D_{sw} R_0}{2A_t} \tag{46}$$

This expression is deduced from expression S_0^0 (Eq. (26)), by considering a flat velocity profile for the velocity $\overline{U_x}$, that is to say independent of r, and by assuming that the azimuthal velocity component $\overline{U_\theta}$ is constant over the entire

radius of the injector. The latter hypothesis may be acceptable with tangential channel holes which are very large, of the order of magnitude of the radius of the injector, but not with tangential holes having a diameter much smaller than the radius of the injector. In [52], this equation was compared with experimental results and it was shown to yield values that overestimate results obtained by integrating velocity profiles and making use of expression S_{conv}. To correct this effect, it was suggested [52] that the azimuthal velocity profile could be represented by a solid body rotation, with $\overline{U_\theta}$ depending linearly on r, yielding an expression $S_{geo,2}$ that was one half of $S_{geo,1}$

$$S_{geo,2} = \frac{\pi D_{sw} R_0}{4A_t} \tag{47}$$

In [52], this expression was found to be in better agreement with experimental determinations of the conventional swirl number S_{conv}.

Chigier and Chervinsky [25] proposed a simplified expression, based on $S^0_{U,BL}$ (Eq. (28)), which indirectly takes into account the pressure correction, via $\overline{U_\theta}$. For a solid body rotation with a uniform axial velocity in the duct, they obtained

$$S_{geo,3} = \frac{(1/2)G}{1-(1/4)G^2} \tag{48}$$

where $G = (\text{Max}\,\overline{U_\theta})/(\text{Max}\,\overline{U_x})$ is the ratio between the maximum values of $\overline{U_\theta}$ and $\overline{U_x}$ in a section of the flow.

Another expression derived by Sheen et al. [53] for a radial swirler with variable pitch blades is particularly appealing because the swirl number is given in terms of volumetric mean values of the azimuthal and axial velocities

$$S_{geo,4} = \frac{3}{4}\frac{<\overline{U_\theta}>}{<\overline{U_x}>} \tag{49}$$

In many cases the swirl number is deduced from geometrical parameters pertaining to the blades that serve to turn the flow, or to the injection holes of the tangential flow in the channel [1, 8, 11]. In the case of axial swirlers for example, one uses the velocity imposed by the blade inclination featuring an angle θ with the injector axis and one considers that the axial velocity has a flat profile in the outlet section of the swirler. Using these approximations in S^0_0 leads to the following expression [9]:

$$S_{geo,5} = \frac{2}{3}\frac{1-(D_{hub}/D_{sw})^3}{1-(D_{hub}/D_{sw})^2}\tan\beta \tag{50}$$

where D_{hub} and D_{sw} are the hub and swirler diameters. In the limit case of a zero hub diameter, this expression may be compared with that defining $S_{geo,1}$. For this one uses the angle of the tangential injected stream in the swirler, and by considering that the entry of the fluid into the swirler is defined by this angle over the entire perimeter. With these assumptions one finds that $S_{geo,5}$ is equal to $(2/3)\tan\theta$, while $S_{geo,1}$ becomes equal to $\sin\theta$. For typical angles, of the order of 45°, the corresponding results are close. One may note, however, that algebraic expressions derived by assuming a certain flow field yield swirl number estimates that often differ from values determined from experimental velocity profiles.

2.4. Limitations in using the various formulations

This review of the literature on swirl number formulations indicates that much effort has been made to define a characteristic dimensionless number that will be constant throughout the flow. An important point to note however, is that depending on the formulation, the different equations for the swirl number (Eqs. (24) to (28) and (40) to (45)) require a set of assumptions to ensure the same invariance properties as S^f_P (Eq. (24)). The high Reynolds number hypothesis is widely used, and justifies that the viscous terms are neglected. It is quite suitable in the case of injectors used in combustors. However, in many practical injectors, there are reductions or expansions in cross-section. In this case, the balance equations (Eqs. (11), (21), (33) and (39)) are no longer valid inside the injector. Choi et al. and Degenève et al. [54, 55] present models for the evolution of the swirl number in such configurations.

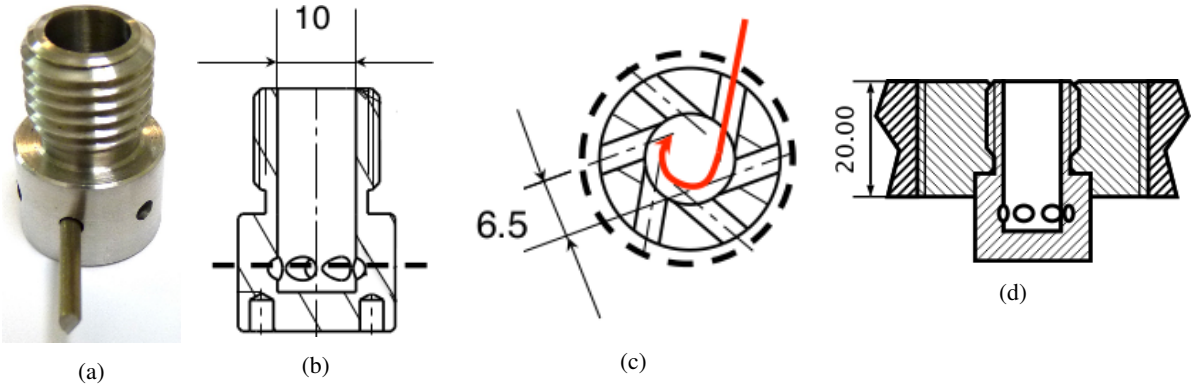

Figure 1: The swirler comprises six tangential channels, which are 3 mm in diameter. (a) Photograph of the swirler. A small rod is placed in one of the holes, (b) Axial cut, (c) Transversal cut at the height indicated by the dashed line in (b). The red arrow shows the air path. (d) Swirler mounted in the combustion chamber backplane. Adapted from [58].

To calculate the swirl number using integral expressions, it is necessary to know the profiles of the different velocity components and the static pressure distribution in the flow. In certain formulations (Eqs. (25), (26) and (28)), the turbulent fluctuations and/or static pressure are eliminated. Some studies [2, 24, 40, 56, 57] have tried to quantify the importance of the neglected terms. Concerning turbulent fluctuations, in [2, 40] the authors have shown experimentally that for high swirl numbers, terms that are usually neglected take significant values. The fluctuations u_r, u_θ and u_x are small but not necessarily negligible compared to the average velocities. It is concluded in these two studies that the turbulent fluctuations could significantly contribute to the axial flow rates used to compute the swirl number. The same authors also investigated the static pressure correction in some peripheral regions of the swirled flow, estimated indirectly using Eq. (15). They found that the static pressure correction could be of the same order of magnitude as $\rho\,\overline{U_x}^2$. In [24, 57], direct measurements of the static pressure are performed using Pitot tubes, and it is shown that the oftentimes neglected pressure term is important to assure the swirl number invariance property. Despite these previous studies, there is still a need to get a precise evaluation of these terms.

Given the experimental difficulties, it is interesting to examine these issues using numerical tools. Because Large Eddy Simulation (LES) methods are considered mature for computing swirling flows, it is timely to carry out a study of a turbulent swirling flow and discuss the various expressions of the swirl number. This is accomplished by examining a generic case in which a swirler is placed in a cylindrical injector connected to a cylindrical chamber. It is thus possible to examine the flow inside the injector unit, in the immediate vicinity of its outlet and in the chamber. The data obtained from calculations will be first validated with Laser Doppler Velocimetry (LDV) measurements.

3. Geometry of the generic swirl injector and description of the numerical scheme

The geometry used in this study corresponds to that of the SICCA combustor, a single injector system operating at EM2C laboratory. The swirling flow can be used to stabilize premixed swirling flames [37, 59–61]. In the present study, all tests are carried out in an isothermal, cold flow configuration, only using air at ambient conditions.

The experimental setup comprises a plenum fed with compressed air through a Bronkhorst EL-Flow mass flow controller, with a relative accuracy better than 0.75%. The plenum ends in a convergent section leading to the swirler. The injector (Fig. 1) comprises a cylindrical channel, of diameter $D_{sw} = 10\,\text{mm}$ and length $L_{inj} = 26\,\text{mm}$, flush mounted on the backplane of the combustion chamber. At the inlet of the swirler, the flow passes through six cylindrical tangential channels of internal diameter $D_{ch} = 3\,\text{mm}$. The axis of the channels is $R_0 = 3.25\,\text{mm}$ away from the axis of the cylinder, and it is located at $x_{channel} = 3.5\,\text{mm}$ above the bottom of the swirler. The combustion chamber is formed by a quartz tube of inner diameter $D_Q = 50\,\text{mm}$ and length $L_Q = 200\,\text{mm}$. A Dantec 2-component Phase Doppler Velocimetry system provides the axial, radial and tangential velocity components.

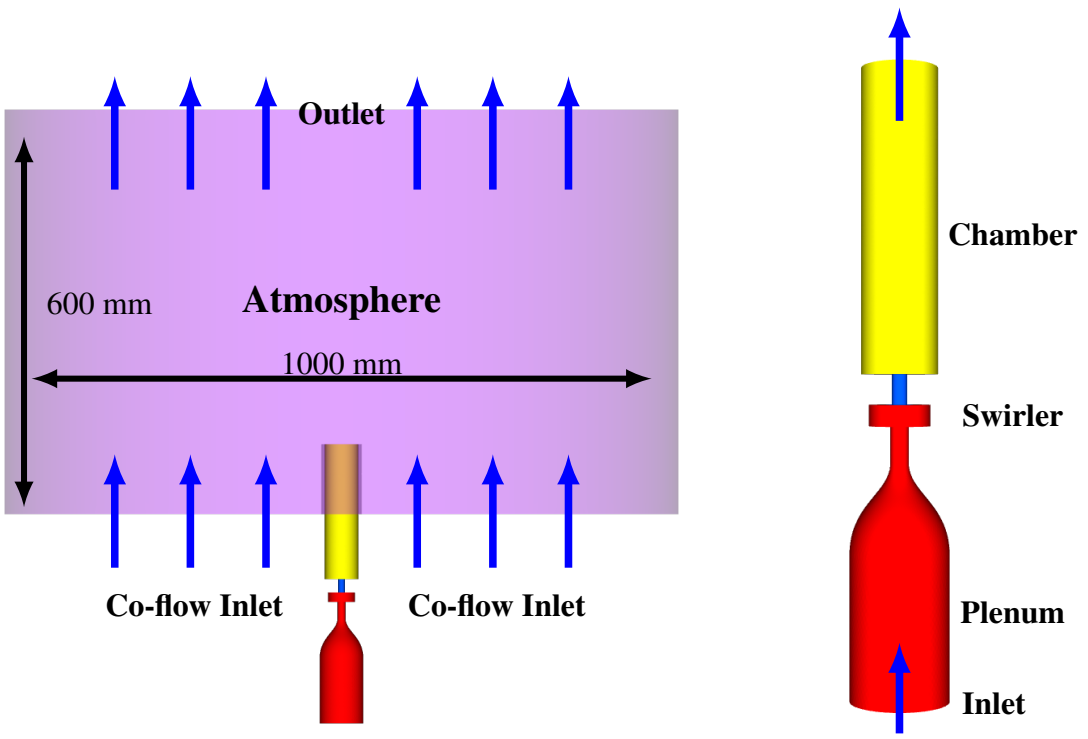

Figure 2: Computational domain; (a) Full domain showing the atmosphere and associated co-flow; (b) Close-up view of the plenum, swirler and combustion chamber; further details may be found in [62]. This figure is adapted from this reference.

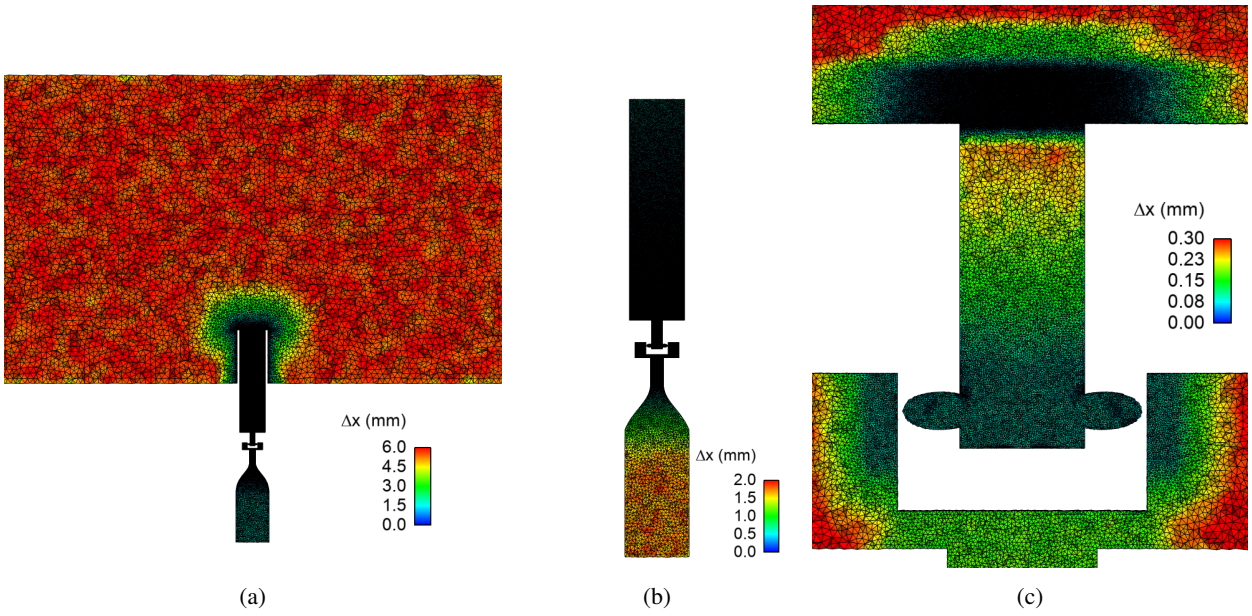

Figure 3: Mesh used for the simulation and element size Δx; (a) Axial cut showing a typical element size of 6 mm in the atmosphere; (b) Axial cut showing element sizes in the plenum ($\Delta x = 2$ mm at the inlet to $\Delta x = 0.3$ mm in the injector). In the chamber, the cell size $\Delta x = 0.25$ mm near the backplane grows quasi linearly to $\Delta x = 0.6$ mm at the chamber outlet; (c) Detailed view of the mesh inside the injector. At the injector outlet the typical cell size is $\Delta x = 50\,\mu$m.

Application of Eqs. (46) and (47) yields the following geometrical swirl number values:

$$\begin{aligned} S_{geo,1} &= 1.2 \\ S_{geo,2} &= 0.60 \end{aligned} \tag{51}$$

For swirling injectors, the Reynolds number is commonly based on the average axial velocity at the nozzle exit and the orifice diameter [21, 40]:

$$\mathrm{Re} = \frac{\langle \overline{U_x} \rangle D_{sw}}{\nu} = 1.11\ 10^4 \tag{52}$$

Numerical simulations are carried out using AVBP, a compressible Navier-Stokes solver developed by CERFACS (https://www.cerfacs.fr/avbp7x). The third order in time and space numerical scheme TTGC [63] is used relying on a two-step Taylor-Galerkin weighted residual central distribution scheme. Subgrid scale turbulence is represented by the SIGMA model [64]. Navier-Stokes Characteristic Boundary Conditions (NSCBC) [65] are employed and set according to the values used in the experiment. The inlet air temperature is set to 298 K, the outlet pressure to $p_{atm} = 101\,325$ Pa. The mass flow rate at the inlet upstream of the swirler is 1.61 g s^{-1}. A logarithmic law of the wall is applied on the solid boundaries[2]. This treatment is preferred to a no-slip condition as the thickness of the laminar sublayer near the wall is estimated to be around $0.1\Delta x$ to $0.25\Delta x$ within the injector, and $0.5\Delta x$ in the chamber (Δx being the characteristic size of a mesh element). Comparison of velocity profiles obtained using the wall law and no slip approach (not shown here) confirmed the choice of the logarithmic law of the wall model.

The computational domain, presented in Fig. 2, comprises the plenum, swirler and combustion chamber. An atmosphere with a slow co-flow is added. The mesh is adapted from Philip [62]. The adaptive mesh refinement (AMR) method of Daviller et al. [67] is used to refine the mesh. Based on the Loss in Kinetic Energy (LIKE) criterion, this AMR method is designed to capture the head loss of swirled injection systems in LES. It is also found in the present configuration to greatly improve the quality of the velocity profiles at the outlet of the injector. A total of 5 steps of AMR are used for this simulation, the parameters for the AMR, defined in [67], are $\alpha = 60$ and $\epsilon = 0.7$. The final mesh comprises a total of 33.55 million tetrahedral elements. The sizes of mesh elements are indicated in Fig. 3.

4. Numerical results and comparison with experiments

4.1. Validation of the simulation

It is first important to ensure that the simulation is reliable by comparing velocity profiles with experimental data acquired with an LDV system downstream of the injector. The injector flow is seeded with micronic silicon oil droplets. Profiles are determined at three heights from the injector outlet, respectively $0.25D_{sw}$, $0.5D_{sw}$ and D_{sw}. The average and RMS velocity are measured every 0.25 mm for each of the three components. With the cylindrical quartz confinement and its high curvature, LDV measurements can only by conducted up to a radial position of $r = 10$ mm, and are additionally very challenging for the radial velocity component, which could not be adequately measured for radial positions exceeding $r = 7$ mm.

The same velocity profiles are extracted from the Large Eddy Simulation, by time averaging over 250 ms. A sample is taken every 20 µs. Assuming that the mean flow is axi-symmetric, a further averaging is performed by rotation around the axis. Comparison between the LES and LDV measurements are shown in Fig. 4, where mean (black) and RMS (red) values of the axial, tangential and radial velocities are compared in three axial sections. The agreement between the mean LDV velocity data and the simulation results is quite good. Concerning the axial velocity U_x, at $x = 0.25D_{sw}$, the velocity peak is predicted at a slightly smaller radius by the simulation, $r^{peak}_{LES} = 5.2$ mm than the measured value, $r^{peak}_{LDV} = 5.45$ mm. The difference approximately corresponds to the resolution of the LDV measurements. The peak velocity at $x = 0.25D_{sw}$ is underpredicted by 4.7%. This small error is still present at $x = 0.5D_{sw}$ but

[2]High Reynolds number approach following the implementation described in [66]: $u^+ = \ln(9.2y^+)/0.41$ for $y^+ > 11.45$, and a linear dependency between u^+ and y^+ for lower values of y^+.

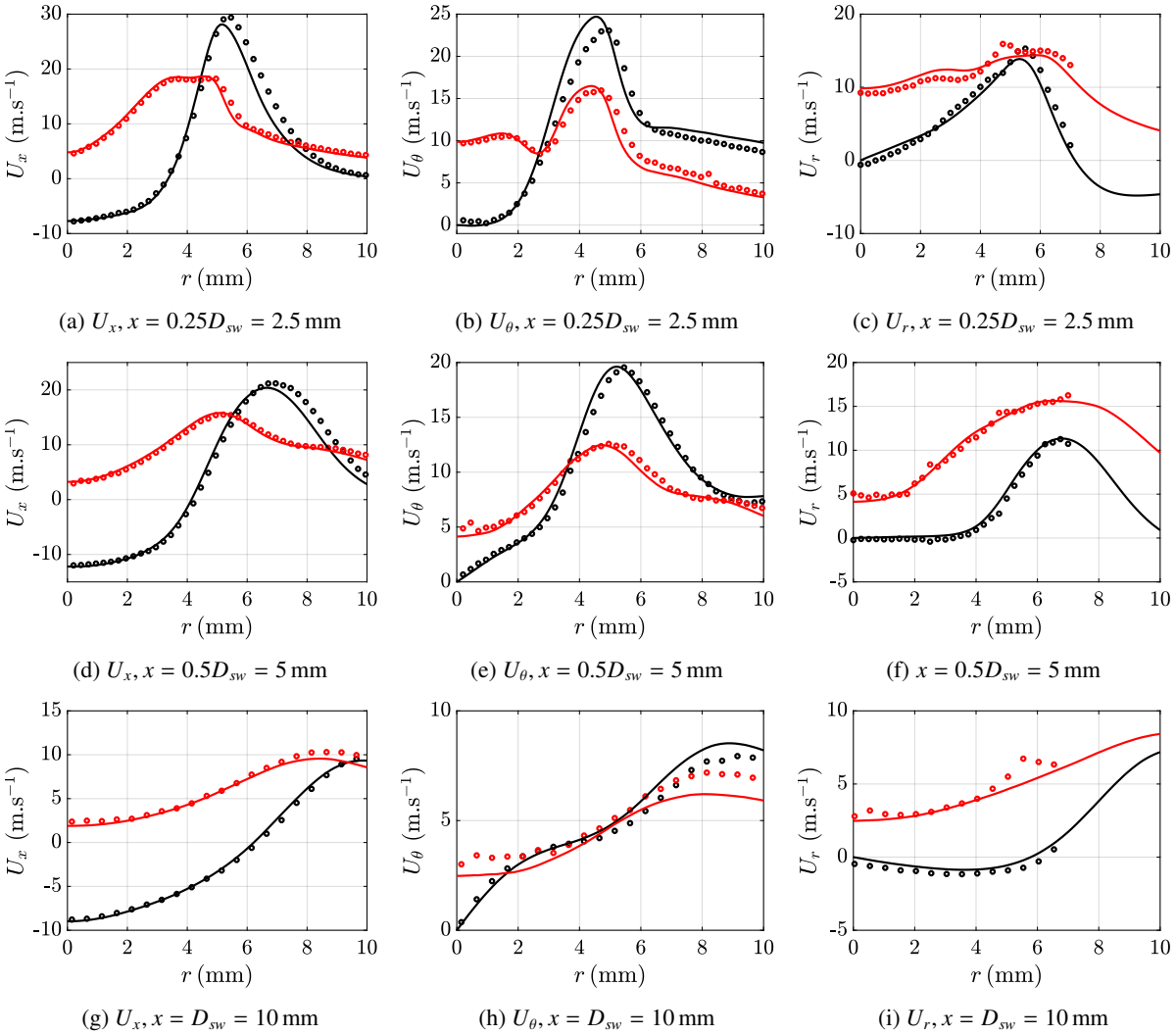

(a) U_x, $x = 0.25D_{sw} = 2.5$ mm (b) U_θ, $x = 0.25D_{sw} = 2.5$ mm (c) U_r, $x = 0.25D_{sw} = 2.5$ mm

(d) U_x, $x = 0.5D_{sw} = 5$ mm (e) U_θ, $x = 0.5D_{sw} = 5$ mm (f) $x = 0.5D_{sw} = 5$ mm

(g) U_x, $x = D_{sw} = 10$ mm (h) U_θ, $x = D_{sw} = 10$ mm (i) U_r, $x = D_{sw} = 10$ mm

Figure 4: Time averaged velocity profiles obtained using LES (continuous lines) and measured with LDV (symbols). Both mean (in black) and RMS (in red) values are shown at three distances from the combustor backplane. From left to right: axial, tangential and radial velocity profiles. Due to the cylindrical geometry of the confinement that the LDV light beams have to cross, measurements are only available up to a radius of 10 mm for U_x and U_θ, and 7 mm for U_r.

becomes vanishingly small further downstream. The peak of the tangential velocity is also predicted 0.45 mm closer to the centerline by the LES, and is overestimated by 6.2% at $x = 0.25D_{sw}$. Further downstream, the agreement is very good for the mean velocities, although the RMS values are underestimated at $x = D_{sw}$. The radial velocities are well predicted by LES, with only a slight underprediction at the highest axial positions.

4.2. General structure of the flow

Colormaps illustrating the general structure of the isothermal flow (Fig. 5) display the three components of the velocity ($\overline{U_x}$, $\overline{U_r}$ and $\overline{U_\theta}$) as well as the pressure ($\overline{p}$), both inside the injection system and in the combustion chamber. Inside the injector, high axial and tangential velocities are found near the periphery. These two components slightly decrease inside the injector. A central low pressure area can be found in the core of the flow. The simplified momentum balance of Eq. (15) explains this nicely. The radial component of the velocity is negligible inside the injector (see Fig. 5(c)).

Near the backplane of the combustor, a hollow cone shaped swirling jet is formed with a recirculation zone at its center. This is well illustrated both in Figure 5(a) and by the black solid line in Fig. 6, which shows the evolution of the axial velocity on the combustor centerline. The recirculating flow is quite strong near the backplane, but starts to decay at $x = 8$ mm. The present vortex breakdown appears to belong to the bubble type geometry rather than to the conical type configuration of Billant et al. [21]. In the conical configuration the cone tip would point towards the injector outlet. This is not the case, one observes however that the bubble is ovoidal and that the upstream part widens rapidly while the downstream region closes more slowly. An outer recirculation zone is also present near the backplane, underneath the jet. Around $x = 20$ mm, the outer layer of the conical jet reaches the side wall. This position is marked in Fig. 5 by a red dotted line. At $x = 35$ mm (white dotted line in Fig. 5), the jet has finished impacting the wall, and the flow starts to stabilize in a slowly evolving state. The pressure mean and wall values in the cylindrical chamber are close to p_{atm}, but still differ by several pascals from each other (Fig. 6). The recirculated massflow rate is shown as the red curve in Fig. 6. A strong recirculation develops immediately downstream of the injector, and the recirculated massflow rate presents a local minimum at $x = 16$ mm. At the same position, the wall pressure has a local maximum, indicating the location of the vortex breakdown. This feature is reminiscent of the results published by Sarpkaya [32] who finds a wall pressure evolution similar to that of Fig. 6, and relates a local maximum in wall pressure to the location of vortex breakdown. In Figure 5(a) and in Fig. 6, on the axis of the injector tube, one can see an elongated zone where the axial velocity $\overline{U_x}$ is weakly negative. This zone delimited by a white line also corresponds to a recirculation, but with a very low flow rate. This region created by the impact of the radial jets coming out of the swirler inside the injector has no influence on the development of the vortex breakdown at the outlet of the injector.

4.3. Instantaneous flow field

The instantaneous velocity and pressure fields within the injector shown in Fig. 7 present the same overall features as the averaged field of Fig. 5. However, they reveal the highly turbulent nature of the flow, and the presence of a precessing vortex core (PVC) within the injector at a frequency of 1740 Hz. On the path of the PVC materialized by the depression zone shifted from the axis (in blue in Figure 7b), it is possible to observe a small zone of negative axial velocities (Fig. 7a). But this recirculation zone fluctuates and does not appear once the data are averaged (Fig.5a). At the bottom of the injection tube one also see a negative velocity zone on the axis. The three recirculation zones: at the inlet of the injection tube, in the PVC and at the outlet of the injection tube remain distinct. There are always positive axial velocity zones between them. The velocity and pressure distributions in the chamber, up to the outlet, are shown in Fig. 8. An important flow feature is the inner, lower pressure recirculation zone extending from the injector to the outlet of the cylindrical combustor. It thus possible to ignite a swirled burner from the outlet of the combustion tube. The flame then propagates from the end of the tube to the outlet of the injector. The transverse cut in Fig. 8(c) shows that the instantaneous recirculation zone is not axisymmetric. This region is precessing at a frequency that is much lower than that of the PVC.

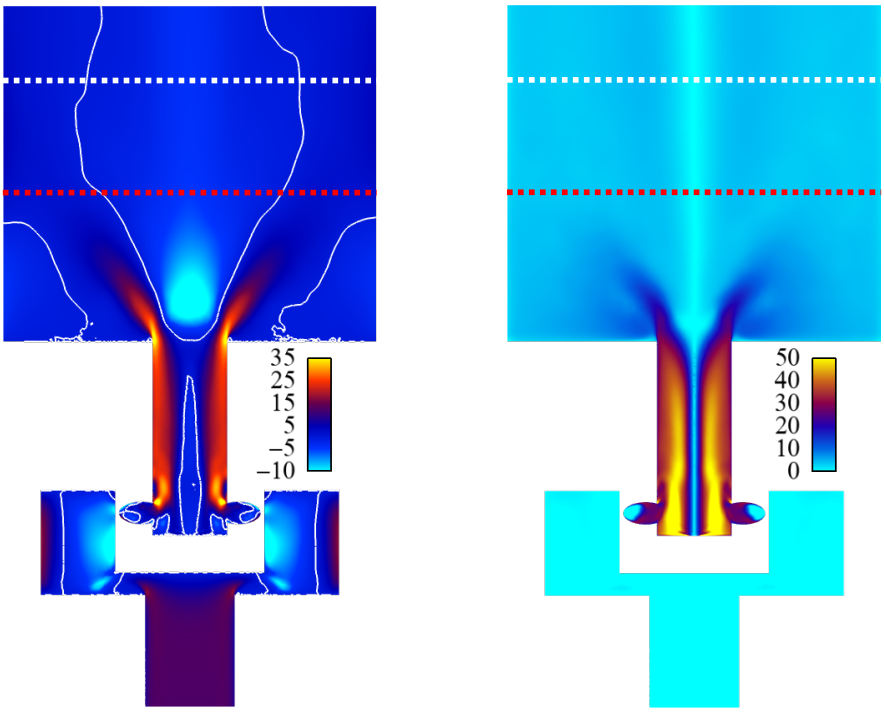

(a) $\overline{U_x}$ (m s^{-1}) (b) $\overline{U_\theta}$ (m s^{-1})

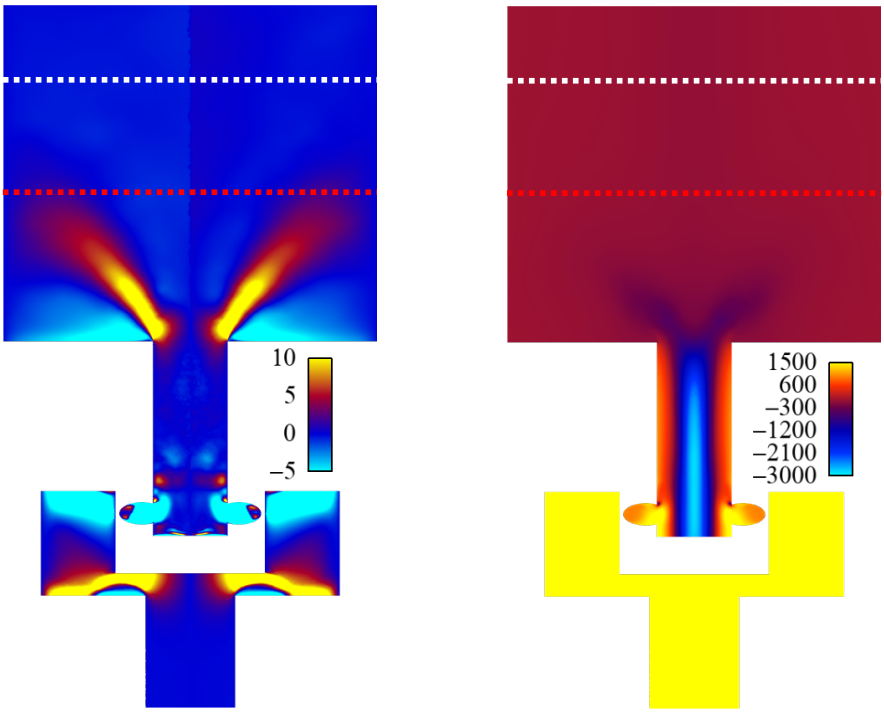

(c) $\overline{U_r}$ (m s^{-1}) (d) $\overline{p} - p_{atm}$ (Pa)

Figure 5: Axial cut showing the local time-averaged values of the three velocity components and of the pressure. On the top left image (a), the white isocontour corresponds to $\overline{U_x} = 0$. For the radial velocity $\overline{U_r}$, the values were saturated at 15 m s^{-1}. Values above this level were only reached in the swirler feeding manifold, which is of little interest for this study. The pressure evolution is represented by $\overline{p} - p_{atm}$. It is saturated at 1500 Pa as higher values are only reached upstream in the plenum. The red dotted line corresponds to a distance $x = 20$ mm from the backplane, and the white dotted line to $x = 35$ mm.

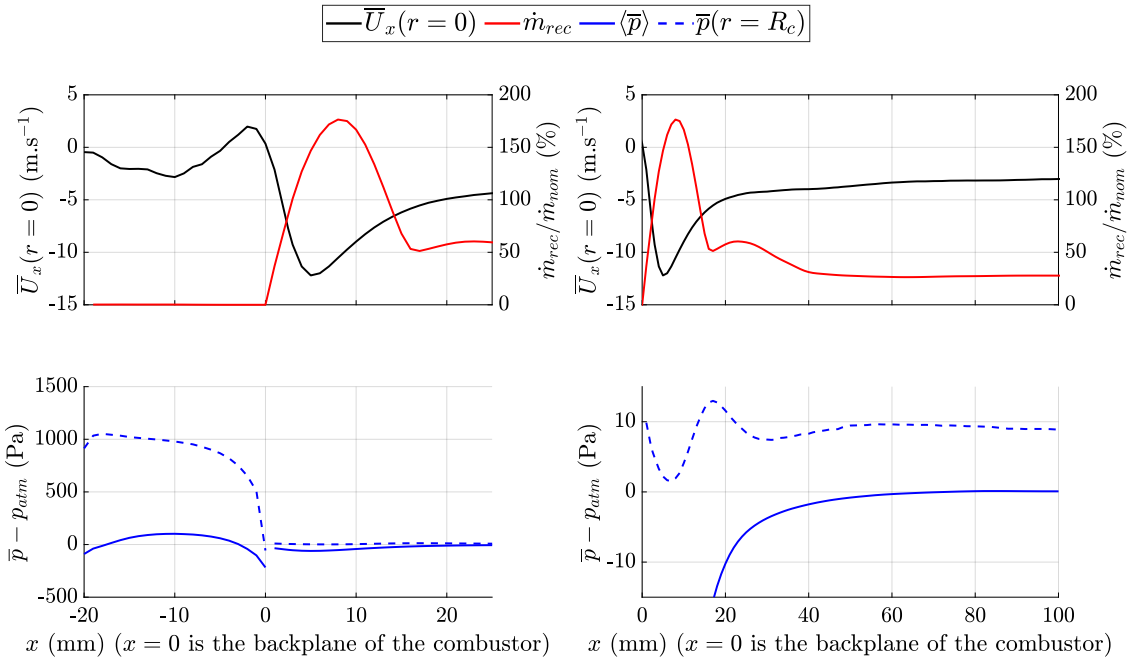

(a) Inside the injector and near-field.

(b) Downstream of the injector.

Figure 6: Top plot, left axis: evolution of the mean axial velocity $\overline{U_x}$ on the centerline (black line); top plot, right axis: recirculating mass flow rate normalized by the nominal flow rate (red line); bottom plot: axial evolution of the section-averaged pressure $\langle\overline{p}\rangle - p_{atm}$ (blue line) and of the pressure at the wall $\overline{p}(r = R_c) - p_{atm}$ (blue dashed line).

4.4. Axial evolution of flow variables

Figure 9 shows the axial evolution of the velocity inside the injector and downstream of the dump plane. Four variables are shown: $\overline{U_x}$, $\overline{U_\theta}$, $\overline{U_r}$ and $\overline{p}$. The four plots on the left (Fig. 9(a)) show radial variations at five locations inside the injector $x = -15\,\text{mm} = -1.5D_{sw}$, $x = -10\,\text{mm} = -D_{sw}$, $x = -5\,\text{mm} = -0.5D_{sw}$, $x = -1\,\text{mm} = -0.1D_{sw}$, and $x = 0$. Strong variations can be observed: for $\overline{U_x}$, the first three profiles ($x = -15...-5\,\text{mm}$) are quite similar, but close to the injector outlet, the inner stagnation zone, precursor to the inner recirculation, widens, and the peak value of the axial velocity strongly increases near the outer wall. $\overline{U_\theta}$ features a similar pattern. Close to the injector outlet and outside the boundary layer, the flow is nearly in solid body rotation. At $x = -15...-5\,\text{mm}$, this solid body rotation behavior can only be seen up to about half the injector radius, with a slow axial decay. As observed in Fig. 5, the radial velocity $\overline{U_r}$ is quite small in the injector. It slightly increases near the outlet. A strong low pressure inner core is present and it rapidly decays near the outlet.

The four plots on the right in Fig. 9(b) display the same variables in six sections on the downstream side of the dump plane: $x = 1\,\text{mm} = 0.1D_{sw}$, $x = 2.5\,\text{mm} = 0.25D_{sw}$, $x = 5\,\text{mm} = 0.5D_{sw}$, $x = 10\,\text{mm} = D_{sw}$, $x = 20\,\text{mm} = 2D_{sw}$ and $x = 80\,\text{mm} = 8D_{sw}$. $\overline{U_x}$ is characteristic of a hollow cone jet. The radial position of the velocity maximum moves outwards and its value decreases as the distance from the dump plane increases. The inner recirculation zone intensifies up to $x = 5\,\text{mm}$ before slowly decaying, as shown in Fig. 6. A weak outer recirculation zone is also slowly forming near the outer wall. $\overline{U_\theta}$ similarly decays and its peak moves outwards as x increases. At $x = 1\,\text{mm}$ and $x = 2.5\,\text{mm}$, a strong, outwardly oriented radial velocity is present near the axis, up to $r = 7\,\text{mm}$, where a strong shear region is established. On the contrary, from this point to the outer wall, a recirculation is present, with an inwardly oriented velocity component. At $x = 5\,\text{mm} = 0.5D_{sw}$ and $x = 10\,\text{mm} = D_{sw}$, the inner recirculation zone weakens, and the radial velocity near the centerline becomes small and oriented inwards. The radial velocity is strongly positive inside the jet and becomes negative in the outer recirculation zone. At $x = 20\,\text{mm} = 2D_{sw}$, the $\overline{U_r}$ velocity profile is much more uniform with a small peak corresponding to the spreading jet and it is completely flat at $x = 80\,\text{mm} = 8D_{sw}$.

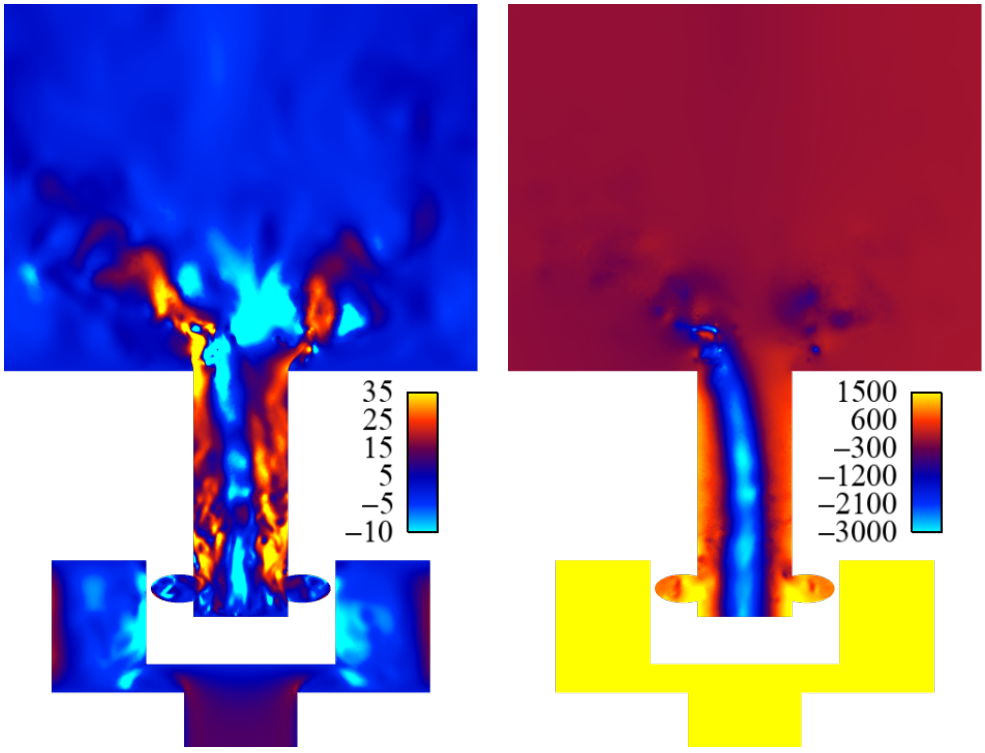

(a) u_x (m s^{-1}). (b) p (Pa).

Figure 7: Axial cut showing instantaneous values of the axial velocity and of the pressure in the injector. Concerning the pressure, the atmospheric pressure p_{atm} = 101 325 Pa has been substracted, and it is saturated at p_{atm} + 1500 Pa as higher values are only reached upstream in the plenum.

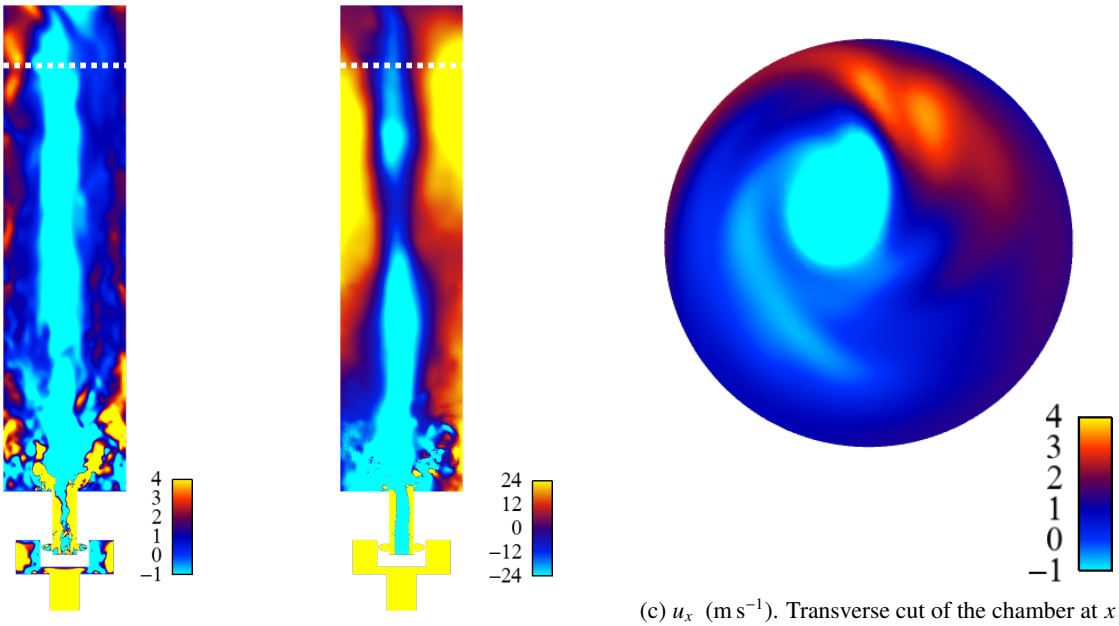

(a) u_x (m s^{-1}). (b) p (Pa). (c) u_x (m s^{-1}). Transverse cut of the chamber at x = 175 mm.

Figure 8: Axial cut showing the local instantaneous values of the axial velocity (a) and of the relative pressure, $p - p_{atm}$ (b) in the chamber. The white dotted line in the chamber corresponds to x = 175 mm, where a transversal cut showing the axial velocity near the outlet is taken and shown in (c).

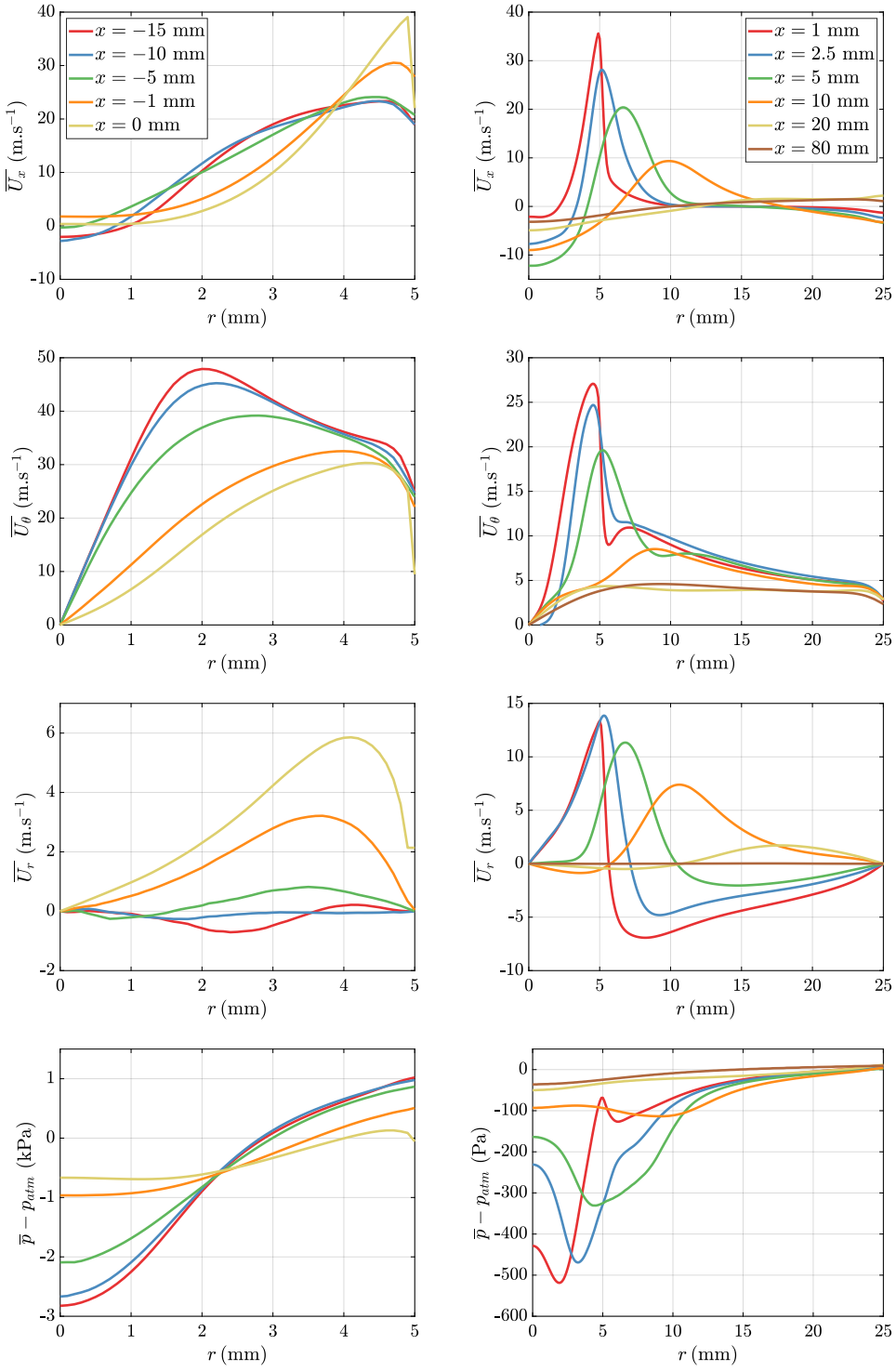

(a) Inside the injector.

(b) Downstream of the injector.

Figure 9: Radial profiles of the mean axial velocity $\overline{U_x}$, tangential velocity $\overline{U_\theta}$, radial velocity $\overline{U_r}$ and pressure $\overline{p} - p_{atm}$. The four plots on the left show these variables for five axial locations inside the injector, the four plots on the right for six axial sections in the chamber.

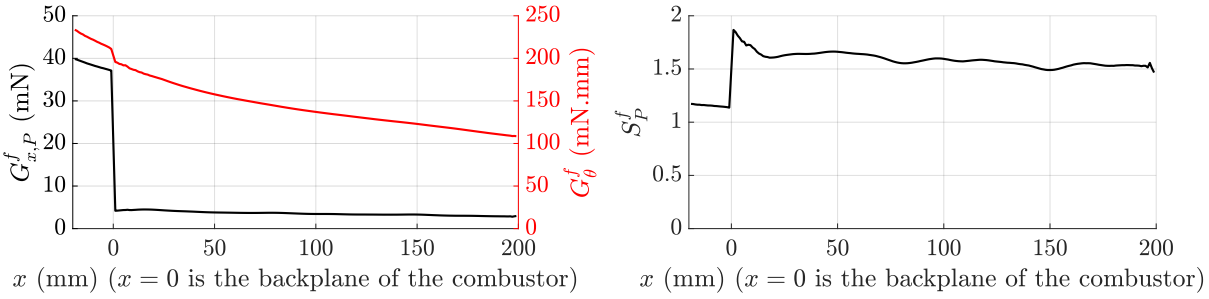

Figure 10: Evolution of the flow rate of axial momentum $G^f_{x,P}$ (left subfigure, left axis, black), of the flow rate of the angular momentum axial component G^f_θ (left subfigure, right axis, red), and the swirl number S^f_P (right subfigure). The reference pressures are set to $p_{ref} = 101\,325.3$ Pa in the chamber ($x > 0$) and $p_{ref} = 101\,405$ Pa inside the injector ($x < 0$). The reference radius is the radius of the confinement: $R = R_c = 5$ mm for $x < 0$ and $R = R_c = 25$ mm for $0 < x < 200$ mm.

The profiles at $x = 20$ mm and $x = 80$ mm are quite similar for all four variables under consideration. Looking at the mean pressure in Fig. 5(d), or comparing the two bottom plots in Fig. 9, the low pressure area at the core of the jet decays rapidly near the injector outlet. At $x = 1, 2.5$ and 5 mm, the pressure profiles reach their minimum in the shear layer formed between the inner recirculation zone and the jet, away from the centerline. This is probably due to the precessing vortex core. Pressure inhomogeneities quickly decay further downstream, leading to a nearly flat pressure profile at $x = 20$ mm and $x = 80$ mm.

The previous calculations pertain to an injector equipped with a radial swirler. One reviewer raised the question of whether the present conclusions would still hold with an axial swirler giving rise to blades trailing edge wakes. This study could not be carried out but one may note that radial and axial swirlers have similar dynamical features (see for example [**?**])

5. The confined flow case

It is now possible to analyze the various expressions used to determine the swirl number and evaluate the simplified formulations presented in section 2. It is first interesting to examine the quasi-invariance of the swirl number in the cylindrical chamber and show that this is only assured if the pressure term is accounted for (subsection 5.1). The second item to consider is that of the determination of the reference pressure p_{ref}. For confined flows, the determination of p_{ref} is not straightforward, a point discussed in subsection 5.2. Since static pressure measurements inside the flow are difficult it is interesting to evaluate alternatives based on velocity measurements (subsection 5.3). Fluctuating velocity terms that are often neglected are evaluated in subsection 5.4. The question of the limits to use for integration is considered in subsection 5.5. These results are finally summarized in subsection 5.6 leading to practical conclusions.

5.1. Axial evolution of the swirl number S^f_P and viscous losses

In this first analysis of the evolution of the swirl number it is convenient to use a reference pressure that is equal to $p_{ref} = 101\,325.3$ Pa in the chamber ($x > 0$), and $p_{ref} = 101\,405$ Pa in the injector ($x < 0$). The reasoning behind this choice will be discussed in the next section 5.2. One may note that this arbitrary choice of reference pressure does not affect the results and reasoning presented in what follows.

One may first consider the axial flow rates and swirl number as originally defined in [23] and in [24] without any simplifying assumptions. $G^f_{x,P}$, G^f_θ and S^f_P are defined in Eq. (40) for a confined isothermal configuration. Their evolutions are shown in Fig. 10. The system comprises two cylindrical tubes of different diameters (see Fig. 2), the radius is constant in the injector ($x < 0$) and in the chamber ($0 < x < 200$ mm) with a sudden expansion between these two at $x = 0$. In this section, the reference radius used for the computation of the swirl number is taken as the actual radius of the confinement at the axial position under consideration: $R = R_c = 5$ mm for $x < 0$ and $R = R_c = 25$ mm

	ΔG^f_θ (mN mm)	$2\pi R_c^2 \int \overline{\tau_{r\theta}}\|_{r=R_c}$ (mN mm)	$\Delta G^f_{x,P}$ (mN)	$2\pi R_c \int \overline{\tau_{rx}}\|_{r=R_c}$ (mN)
Injector: $-20\,\text{mm} < x < 0$	-23	-17	-2.8	-2.8
Chamber: $0 < x < 200\,\text{mm}$	-87	-66	-1.3	-1.3

Table 1: Decay in G^f_θ and $G^f_{x,P}$ along with viscous losses at the wall in the injector and in the chamber.

for $0 < x < 200\,\text{mm}$. There is a sizable jump in $G^f_{x,P}$, and a very small jump in G^f_θ at the position of sudden expansion ($x = 0$). These two quantities slowly decay in the constant section ducts. Correspondingly S^f_P also features a jump at $x = 0$ and then slowly diminishes in the axial direction reflecting the observed reductions in G^f_θ and that of $G^f_{x,P}$.

At this point it is interesting to discuss the decay observed in the flow rate of the angular momentum axial component by first reviewing studies dealing with turbulent swirling flows decay in tubes. This topic is covered for example by Steenbergen and Voskamp [7] who review different formulas for this evolution, but give their results in terms of swirl angle instead of swirl number. The linearized theory in [68] for established turbulent swirling flows in long pipes indicates a typical decay of 10 to 20% on a distance of 50 pipe diameters. The decay rate increases at lower Reynolds number. Scott and Bartelt [69] note the invariance of the velocity profiles in the axial direction in an experiment on a annular duct with a swirling air flow. Kitoh [70] provides an experimental assessment of the wall shear stress impact and concludes that it governs the decay of the swirling motion which is generally found to be exponential. Another relevant feature from these studies is that the decay of axial component of the flow rate of angular momentum G^f_θ predominates over that of the flow rate of axial momentum $G^f_{x,P}$, in agreement with the theoretical analysis of Reynolds [28].

In this respect it is worth recalling the rates of change balances of G^f_θ and $G^f_{x,P}$ established in section 2, Eqs. (33) and (39). These expressions indicate that the decay rates of G^f_θ and $G^f_{x,P}$ are governed by the shear stresses at the wall. The order of magnitude of these stresses is such that the decay rate of G^f_θ is much larger than that of $G^f_{x,P}$.

It is next interesting to examine the decay of G^f_θ and $G^f_{x,P}$ in the injector and in the chamber, as well as the friction losses at the wall, reported in Tab. 1. As the literature suggests, it appears that friction losses associated with wall stresses determine the slow axial decay of the swirl number.

5.2. Impact of the static pressure on the swirl number and selection of the reference pressure

Let us now evaluate the impact of the pressure term on $G^f_{x,P}$. This issue was considered in the past by Chigier and Beér [24] and Mahmud et al. [57] who used Pitot tubes to measure velocity and static pressure profiles in free swirling jets. It was found in these previous studies, in agreement with the theoretical equation Eq. (11), that the pressure term had to be included to ensure the axial conservation of $G^f_{x,P}$. This question may now be examined with the present simulation thus avoiding intrusive pressure measurements. It is interesting to separate $G^f_{x,P}$ in its constituents

$$\underbrace{G^f_{x,P}}_{\text{(black)}} = \underbrace{2\pi \int_0^{R_c} \rho \left[\overline{U_x}^2 + \overline{u_x^2}\right] rdr}_{\text{Velocity term (red)}} + \underbrace{2\pi \int_0^{R_c} \left[\overline{p} - p_{ref}\right] rdr}_{\text{Pressure term (blue)}} \tag{53}$$

Figure 11 indicates that $G^f_{x,P}$ and $G^f_{x,0} = 2\pi \int_0^{R_c} \rho \left[\overline{U_x}^2 + \overline{u_x^2}\right] rdr$ nearly coincide in the injector ($x = -20$ to $0\,\text{mm}$) and in the downstream region of the chamber ($x = 50$ to $175\,\text{mm}$) with the choice of p_{ref} that is employed here. However, as observed in [57], these quantities take different values in the vicinity of the area changes. Near $x = 0$, $G^f_{x,0}$ features a peak and sizable variations caused by the recirculation region generated by vortex breakdown. The pressure term $2\pi \int_0^{R_c} \left[\overline{p} - p_{ref}\right] rdr$ also features a strong negative peak at this position. The two peaks compensate each other when

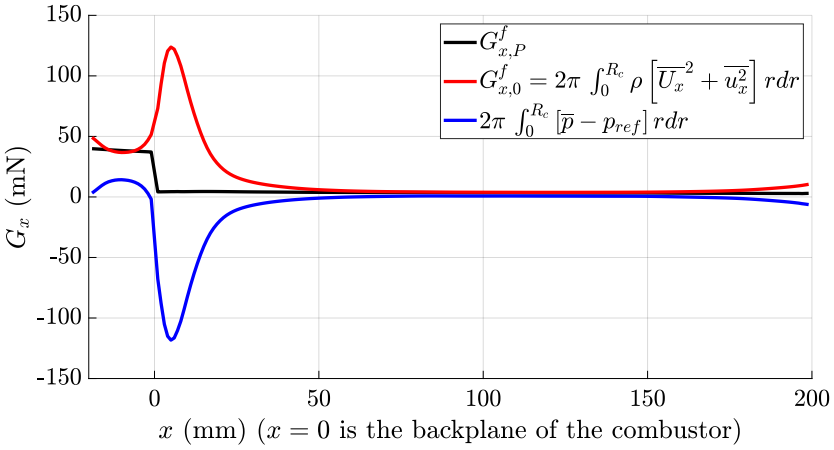

Figure 11: Evolution of $G^f_{x,P}$ and its constituents (Eq. (53)) in the axial direction. The sudden expansion corresponds to $x = 0$. The reference pressures are set to $p_{ref} = 101\,325.3$ Pa in the chamber ($x > 0$) and $p_{ref} = 101\,405$ Pa inside the injector ($x < 0$).

the two terms are summed up in $G^f_{x,P}$. This indicates that the pressure term is of considerable importance close to area changes ($0 < x < 50$ mm) to ensure conservation, but that this term can be omitted where the flow is established ($-20 < x < 0$ mm and $50 < x < 175$ mm).

The selection of a reference pressure is rarely considered in the previous literature but a suitable choice needs to be made because $G^f_{x,P}$ is sensitive to changes in reference pressure with a first order impact on the swirl number value. For the purpose of swirl number calculations, $\rho\left(\langle\overline{U_x}\rangle^2 + \langle\overline{u_x^2}\rangle\right)$ gives the order of magnitude for the sensitivity of the swirl number to the reference pressure. In the present configuration, $\rho\left(\langle\overline{U_x}\rangle^2 + \langle\overline{u_x^2}\rangle\right) \approx 0.5$ Pa in the confinement tube. From a practical standpoint, Mattingly and Oates [47] propose to use a pressure at the wall somewhere in the duct as reference pressure, but with no theoretical justification. One may note that, from Fig. 6, the pressure at the wall varies as a function of the axial position x, and that the difference between the section averaged pressure $\langle\overline{p}\rangle$, and the wall pressure $\overline{p}(r = R_c)$ is approximately $\overline{p}(r = R_c) - \langle\overline{p}\rangle \approx 9$ Pa for $x > 40$ mm, that is one order of magnitude larger than $\rho\left(\langle\overline{U_x}\rangle^2 + \langle\overline{u_x^2}\rangle\right)$. The practice of taking the reference pressure as a wall pressure without selecting a suitable section in the flow is inadequate, in particular for flows with changes in cross-section. This leads to variable or even sometimes negative swirl number values [12] depending on the position adopted to infer the reference pressure.

The following analysis is dedicated to defining a better practice for this choice. The following properties are desirable for the reference pressure p_{ref}:

[P1] Its definition should be consistent with that used for unconfined flows,

[P2] Its value might vary with area changes, but should remain constant in the system elements having a constant cross section,

[P3] Its determination should be straightforward using conventional measurement techniques,

[P4] Its value should be such that $G^f_{x,P} \simeq G^f_{x,0}$ at a distance from the area change where the flow is established as illustrated in Fig. 11.

If it is to have properties [P4], the reference pressure must be defined as the sectional average of the static pressure

$$p_{ref} = \langle\overline{p}\rangle = \frac{1}{\Sigma}\int_\Sigma \overline{p} dA \tag{54}$$

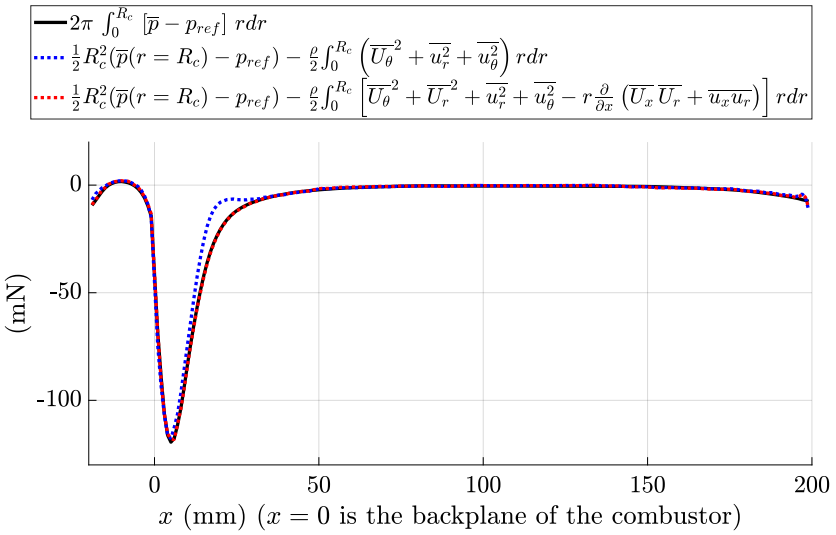

Figure 12: Axial evolution of different pressure correction expressions. Blue, Eq. (35); red, Eq. (56). The reference line is in black. p_{ref} = 101 325.3 Pa in the chamber ($x > 0$) and p_{ref} = 101 405 Pa inside the injector ($x < 0$).

where Σ designates the cross-section where the reference pressure is computed. In this expression, if Σ becomes infinitely large, for example if an unconfined swirling jet is considered, the reference pressure will simply tend to the pressure at infinity p_∞.

$$\lim_{\Sigma\to\infty} p_{ref} = p_\infty = \overline{p}(r \to \infty) \tag{55}$$

The definition of the reference pressure proposed in Eq. (54) is thus consistent with Chigier's definition for unconfined swirling jets and satisfies property [P1]. Property [P2] imposes that this sectional average be taken at a single axial location in each part. In the present configuration, the sectional average of static pressure is nearly constant in the downstream part of the duct after an establishment distance roughly corresponding to the confinement diameter. This property can most likely be generalized to many constant pressure combustion applications featuring constant cross-sections due to the high Reynolds number and small length to diameter ratios that are generally found in combustors.

The reference pressure is thus taken as the mean value of the cross-section averaged static pressure at positions ($-15 < x < -5$ mm for the injector and $50 < x < 175$ mm for the chamber), that is at least one diameter downstream of area changes and at a distance from an outlet to avoid end effects. This yields $p_{ref}(-)$ = 101 405 Pa in the cylindrical injector and $p_{ref}(+)$ = 101 325.3 Pa in the downstream duct. Figures 10 and 11 use the previous reference pressures and show that $G^f_{x,P}$ and G^f_θ evolve in the axial direction in the expected manner and that $G^f_{x,P}$ and $G^f_{x,0}$ collapse where the flow is fully developed.

5.3. Expressing the static pressure in terms of the velocity field and wall pressure

It is not always easy to measure the static pressure inside the flow with a sufficient resolution to correctly evaluate the pressure term in Eq. (53). Among the methods that can be used to replace this by an expression that only uses velocity information, it is interesting to examine that originally proposed by Chigier and Chervinsky [25] for free swirling jets and extended by Mattingly and Oates [47] for confined configurations. It is expressed in Eq. (35)It is worth noting that, in confined flows, this formulation still requires a wall pressure measurement $\overline{p}|_{r=R_c}$. It is useful at this point to recall that this expression is derived from the simplified Navier-Stokes equations with boundary layer assumptions

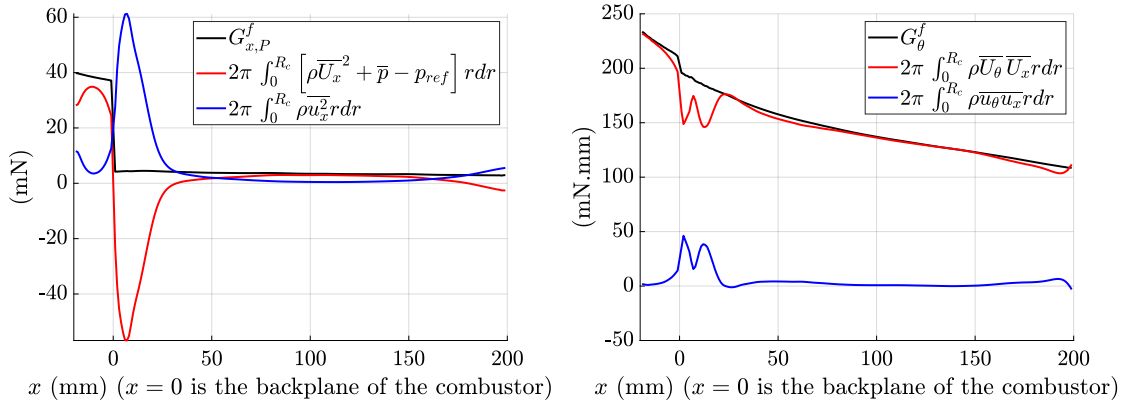

Figure 13: The different components of the flow rate of axial momentum (left) and axial component of the flow rate of angular momentum (right). p_{ref} = 101 325.3 Pa in the chamber ($x > 0$) and p_{ref} = 101 405 Pa inside the injector ($x < 0$).

(Eq. (13)) and that terms that depend on the radial velocity may also be included to get a more general expression

$$\begin{aligned} \int_0^{R_c} r\,(\overline{p} - p_{ref})\,dr &= \frac{1}{2}{R_c}^2(\overline{p}|_{r=R_c} - p_{ref}) \\ -\frac{\rho}{2}\int_0^{R_c} r\left[(\overline{U_\theta}^2 + \overline{U_r}^2 + \overline{u_r^2} + \overline{u_\theta^2}) - r\,\frac{\partial}{\partial x}\left(\overline{U_x}\,\overline{U_r} + \overline{u_x u_r}\right)\right] dr & \end{aligned} \tag{56}$$

Figure 12 shows the axial evolution of $\int_0^{R_c} r\,(\overline{p} - p_{ref})\,dr$ and the two expressions appearing in Eqs. (35) and (56). Equation (35), commonly found in the literature, yields suitable results except between x = 5 mm and 30 mm, where the boundary layer assumptions do not apply. This might explain the unexpected swirl number measurements put forward by Mattingly and Oates [47]: when measuring the swirl number in a pipe downstream of a swirling injector, they found that the swirl number $S^0_{U,BL}$ was nearly constant, expect in the vicinity of the injector outlet where it notably differed from its far-field value. Given the sensitivity of the computation of the swirl number to the pressure, it is then preferable to use Eq. (56) in the injector near-field.

5.4. Fluctuating terms

It is now worth asking whether the terms corresponding to the fluctuating velocities need to be included. It is shown by Toh et al. [40] using PIV data that neglecting these terms only induced a 3% error in the swirl number because the errors in the numerator and denominator compensate each other. It should be noted that these authors did not have access to all the necessary components in the Reynolds stress tensor.

It is then worth examining this issue by isolating the fluctuating terms in the calculation of $G^f_{x,P}$ and G^f_θ:

$$\underbrace{G^f_{x,P}}_{\text{(black)}} = \underbrace{2\pi \int_0^{R_c} \left[\rho\overline{U_x}^2 + \overline{p} - p_{ref}\right] rdr}_{\text{Mean term } G^0_{x,P} \text{ (red)}} + \underbrace{2\pi \int_0^{R_c} \rho\overline{u_x^2} rdr}_{\text{Fluctuating term (blue)}} \tag{57}$$

$$\underbrace{G^f_\theta}_{\text{(black)}} = \underbrace{2\pi \int_0^{R_c} \rho\overline{U_\theta}\,\overline{U_x} rdr}_{\text{Mean term (red)}} + \underbrace{2\pi \int_0^{R_c} \rho\overline{u_\theta u_x} rdr}_{\text{Fluctuating term (blue)}} \tag{58}$$

These components are shown in Fig. 13. The integral of the fluctuating term $2\pi \int_0^{R_c} \rho\overline{u_x^2} rdr$ is nearly of the same order of magnitude as $G^0_{x,P}$ between $0 < x < 35$ mm. For the axial component of the flow rate of angular momentum G_θ,

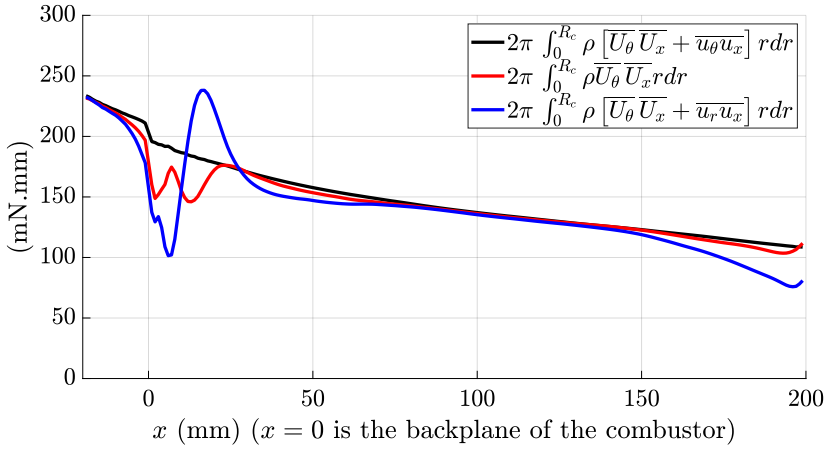

Figure 14: Assessment of the replacement of $\overline{u_\theta u_x}$ by $\overline{u_r u_x}$ in the computation of G_θ^f.

the fluctuating term represents up to 25% of G_θ^f. In view of their importance in the computation of the swirl number and the fact that hot wires or laser velocimetry give access to fluctuating velocities it appears advisable to include the corresponding terms in swirl number calculations, especially for systems such as combustion injectors which operate at high Reynolds numbers.

The experimental determination of $\overline{u_\theta u_x}$ may be based on cross hot wires, two component LDV systems or three component stereo-PIV. The standard 2D-PIV cannot be used to determine this cross-correlation. To overcome this difficulty with this last technique it is suggested in [40] to simply replace $\overline{u_\theta u_x}$ by $\overline{u_r u_x}$. This possibility is assessed in Fig. 14, which compares $2\pi \int_0^{R_c} \rho \left[\overline{U_\theta U_x} + \overline{u_\theta u_x}\right] rdr$, $2\pi \int_0^{R_c} \rho\, \overline{U_\theta U_x} rdr$ and $2\pi \int_0^{R_c} \rho \left[\overline{U_\theta U_x} + \overline{u_r u_x}\right] rdr$. This plot indicates that it is clearly preferable to drop the correlation $\overline{u_\theta u_x}$ than to try to replace it by $\overline{u_r u_x}$.

5.5. Integration limits

Up to now, the integrals defining $G_{x,P}^f$ and G_θ^f have been calculated over the entire cross-section of each element. It is now worth estimating the impact of stopping the computation of the integral at an earlier point. One may consider for that purpose Fig. 15 where $G_{x,P}^f$ and G_θ^f are calculated by integrating to an arbitrary radius R_{lim}:

$$G_{x,P}^f(x, R_{lim}) = 2\pi \int_0^{R_{lim}} \left[\rho\left(\overline{U_x}^2(x,r) + \overline{u_x^2}(x,r)\right) + \overline{p}(x,r) - p_{ref}\right] rdr \tag{59}$$

$$G_\theta^f(x, R_{lim}) = 2\pi \int_0^{R_{lim}} \rho\left(\overline{U_x}(x,r)\overline{U_\theta}(x,r) + \overline{u_x u_\theta}(x,r)\right) r^2 dr \tag{60}$$

Depending on the axial position at which the computation is performed, two regimes can be found. For $x = 2.5, 5$ and 10 mm, Fig. 9 indicates that the flow behaves as a jet with an outer recirculation zone. At $x = 20$ and 80 mm, the flow is wall-bounded and there is no outer recirculation zone. At $x = 2.5, 5$ and 10 mm, the flow rate of axial momentum $G_{x,P}^f$ is initially negative before strongly increasing at the radial position of the jet. It then decays again before increasing to its final value near the wall. G_θ^f has a similar behavior, with a strong increase at the radial position of the jet, followed by a plateau and a decay to its final value in the outer recirculation zone near the wall. At $x = 20$ and 80 mm, both $G_{x,P}^f$ and G_θ^f reach their final values in the last 5 to 10 mm of the confinement. These calculations indicate that in the case of a confined configuration, especially when an outer recirculation zone is established, the computation of the swirl number S_P^f needs to be carried out by integrating over the entire cross-section.

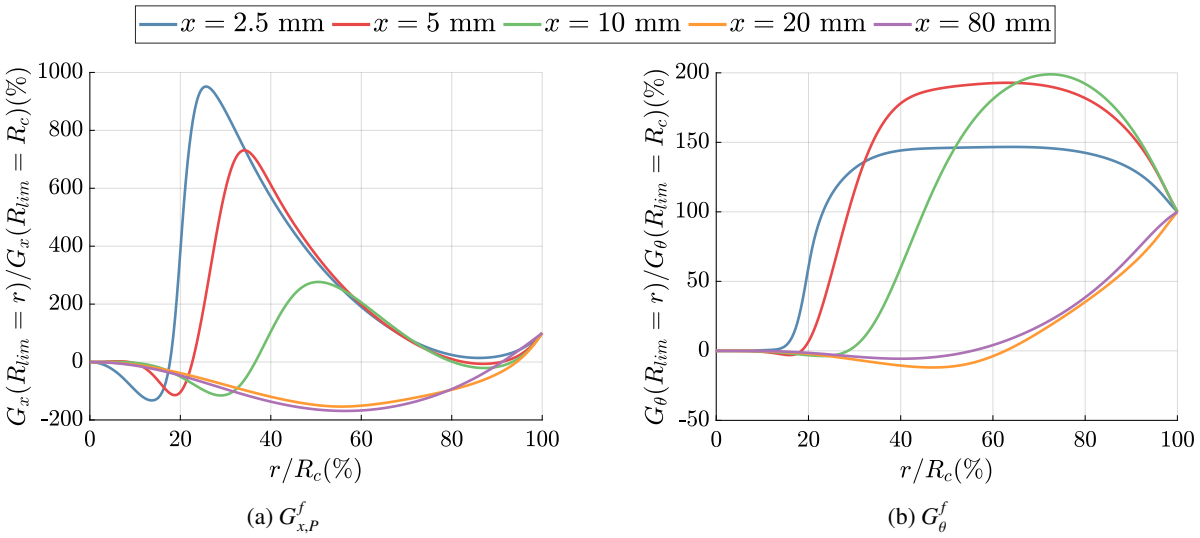

(a) $G^f_{x,P}$ (b) G^f_θ

Figure 15: Effect of integration limit on the calculated flow rates $G^f_{x,P}$ (left) and G^f_θ (right) at five axial positions. The integral terms are computed by stopping the integration at various distances r, and then normalizing by the integral taken over the entire cross-section. p_{ref} = 101 325.3 Pa.

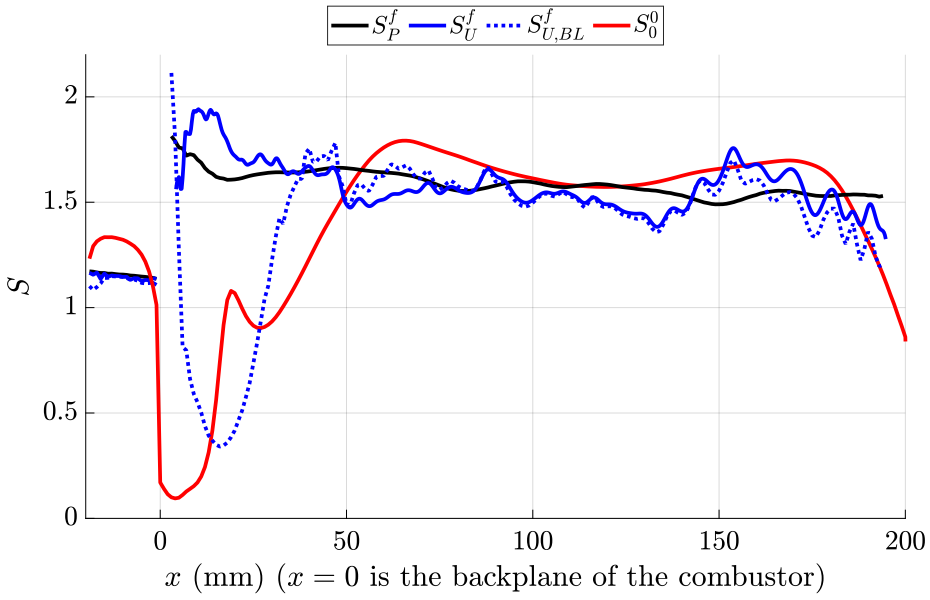

Figure 16: Comparison of 4 formulas for the swirl number.

5.6. Direct comparison of swirl number formulations

Finally, we compare in this section the swirl numbers calculated with the different formulations. The reference pressures are those determined previously in section 5.2. The reference swirl number S_P^f defined by Rose [23] and Chigier et al. [24–26] corresponds to Eq. 40. It includes the pressure and fluctuation terms and appears as a solid black line in Fig. 16. This quantity has the nice feature of being nearly constant in the injector and slowly diminishing in the chamber.

In the second formulation S_U^f corresponding to Eq. (44) the pressure term is replaced by a velocity term and the pressure at the wall. This expression put forward in the present investigation does not appear in the literature. Its derivation relies on the balance put forward in Eq. (56). The boundary layer simplifying assumptions are not needed in this case so that S_U^f, shown as a solid blue line in Fig. 16, takes values that are close to the reference swirl number (black line).
On the other hand, the simplified formulation of Mattingly and Oates [47], $S_{U,BL}^f$, defined in Eq. (43) relies on boundary layer assumptions. Plotted as a dotted blue line in Fig. 16, $S_{U,BL}^f$ is in good agreement with the reference swirl number S_P^f, except in the vicinity of the sudden expansion.

The commonly used, highly simplified expression S_0^0 corresponding to Eq. (42) appears as a red line in Fig. 16. With the definition of the reference pressure proposed in the present work, it is close to S_P^f at axial positions that are far away from area changes. It is also close to S_P^f at $x = 0$, but exhibits large variations in the downstream flow and substantially differs from the reference value S_P^f.

The fairly common expression S_U^0 (where the pressure is replaced in terms of the velocity field, velocity fluctuations are neglected and the reference pressure is set equal to the wall static pressure) corresponding to Eq. (45) is not plotted in Fig. 16 because it becomes negative at some axial sections and its value often exceeds the limits set for the y-axis in this figure. As previously noted by Weber and Dugué [12], this expression is highly variable near the sudden expansion and becomes negative in the downstream section, indicating that the reference pressure is not well chosen. Overall, this is not a suitable approximation of the original swirl number S_P^f.

One may draw the following conclusions from the analysis conducted so far:

- The swirl number S_P^f is a well defined quantity that has desirable conservation properties in many isothermal configurations.
- Although it can be easily determined from numerical simulations its determination from experimental velocity measurements in practical configurations is challenging.
- S_U^f is the most general approximation of S_P^f. The simpler expression $S_{U,BL}^f$ constitutes a good alternative in regions where the flow is established.
- In confined flows, care should be taken to properly define the reference pressure p_{ref}.

6. The conventional swirl number and its estimation

Given the complexity involved in the accurate estimation of the original swirl number S_P^f, it is now interesting to consider the conventional swirl number formulation (Eq. 30) that is widely used in practice to deduce an estimate from velocity profiles measured as close as possible to the injector outlet.

$$S_{conv} = \frac{\int_0^{R_{lim}} \rho\, \overline{U_\theta}\, \overline{U_x}\, r^2 dr}{R_{inj} \int_0^{R_{lim}} \rho\, \overline{U_x}^2\, r dr} \qquad (30\ rep.)$$

In Eq. (30) the reference radius is that of the injector outlet and the integration is stopped at a radial distance R_{lim}. A critical aspect is the suitable choice of this limit. This may be guided by plotting $G_{x,0}^0$, G_θ^0 and S_{conv} calculated in the

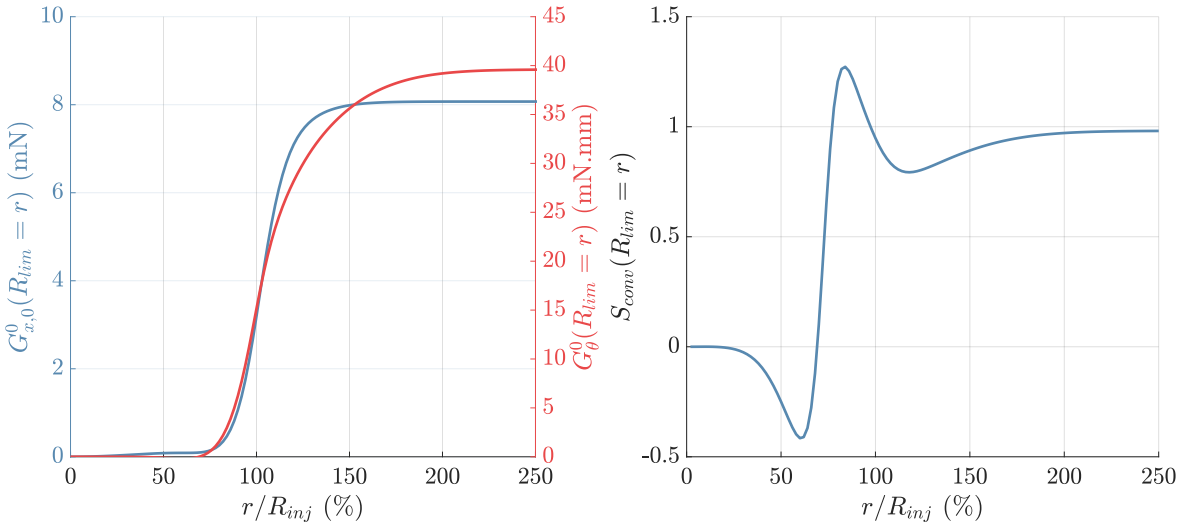

Figure 17: Choice of the integration limit R_{lim} for the computation of the conventional swirl number S_{conv} (Eq. (30)). Velocity profiles are taken at $x = 2.5$ mm. On the left, $G^0_{x,0}$ and G^0_θ are plotted for different integration radii. On the right, the conventional swirl number S_{conv} is plotted in a similar manner.

vicinity of the outlet for different integration radii. Figure 17 indicates that these three quantities become independent of the integration radius as soon as $R_{lim} > 2R_{inj}$. Although the specific value of $R_{lim} = 2R_{inj}$ may depend on the configuration, one may expect that S_{conv} will be independent of the integration radius if R_{lim} is large enough, since the axial velocity component $\overline{U_x}$ vanishes close to the backplane at large radial positions ($r \gg R_{inj}$). In the section located at $x = 2.5$ mm, one finds that S_{conv} takes a value of 0.98 that is close to that obtained for S^f_P near the injector outlet on the upstream side: $S^f_P = 1.14$.

It is clear from the elements presented in the previous section that S_{conv} is weakly related to the original definition and that it does not have the same degree of generality as S^f_P. It is quite dependent on the configuration and on the height above the backplane at which the velocity profiles are measured. This measurement position should be systematically specified along with the integration limit R_{lim} when S_{conv} is quoted. However, since S_{conv} is close to the value of S^f_P inside the injector it may serve to classify injectors and in this sense constitutes a useful characteristic number and a practical alternative to S^f_P.

One should note that the geometrical formula of [50, 51] $S_{geo,1} = 1.2$ (Eq. (46)) which is designed for this specific swirler arrangement and does not rely upon an assumption of a certain shape for the velocity profile, gives a result that is close to S^f_P inside the injector, but also to the conventional swirl number $S_{conv} = 0.98$.

7. Conclusion

This article provides an overview of the hierarchy of simplified definitions derived in the literature to determine the swirl number in practical flows, assesses the shortcomings of the various formulations and advises on which definitions to use in practice. This evaluation is based on a large eddy simulation of a generic system comprising an injector having a circular cross-section, a cylindrical chamber and a sudden expansion between these two elements. This allows a detailed analysis of the various terms involved in the definition of the swirl number. The analysis is first carried out on the swirl number S^f_P originally defined as the ratio of the axial component of flow rate of angular momentum G^f_θ to the axial flow rate of axial momentum $G^f_{x,P}$. It is found that the axial flow rate of axial momentum $G^f_{x,P}$ is nearly constant when the duct section is constant. The decay of the flow rate of G^f_θ is controlled by the

moment of tangential shear stress at the duct wall. The analysis indicates that the swirl number S_P^f defined by Rose, Chigier and co-authors [23–26] needs to account for the pressure term that is often neglected. In practical confined flows this requires the inclusion of a reference pressure. It is shown that this quantity needs to be adapted to each duct element composing the system. The analysis also indicates that it is important to include terms corresponding to turbulent fluctuations in the flow and that these terms correspond to non negligible contributions to the integrated fluxes appearing in the definition of the swirl number. It also appears that all integrations should be carried out up to the wall of the system. The commonly used formula S_U^0 (Eq. (45)) is found to yield inadequate results in the entirety of the system, while $S_{U,BL}^f$ (Eq. (43)) and S_0^0 (Eq. (42)) can only be used at a distance from area changes, in regions where the flow is established. Given these elements, the determination of the original swirl number from experimentally measured velocity profiles is quite challenging and requires the use of the complex expression S_U^f (Eq. (29)), introduced in the present study. Calculating S_U^f requires the measurement of the axial gradient of $\overline{U_x U_r}$ and the wall pressure as well to deduce a reference pressure. In this respect, numerical simulations, which have shown their capability to model swirling flows, appear better suited to the task of determining the original swirl number S_P^f than using formulations that try to approximate the original expression. A highly simplified expression for a conventional swirl number S_{conv} obtained by eliminating the pressure term and the turbulent fluctuation stresses may constitute a practical alternative when the swirl number has to be determined from experimental data. Although it is only weakly linked to the original definition, and does not have the same degree of generality, this conventional swirl number provides an estimate of the degree of swirl and may serve to categorize injectors. Appendices A and B contain a synthesis of recommended practices for the computation of the swirl numbers S_P^f and S_{conv} from experimental measurements and numerical simulations.

Acknowledgments

This work was partially supported by Safran Tech and the FASMIC project of the French Agence Nationale de la Recherche (ANR, grant FASMIC ANR-16-CE22-0013). The authors wish to thank J.M. Dupays for the technical support on AVBP, Dr. M. Philip for providing the geometry of the numerical domain, Pr. F. Baillot, Pr. R. Vicquelin and Dr. A. Degenève for helpful discussions on the swirl number and numerical setup. CERFACS is also acknowledged for the use of the AVBP solver. This work was granted access to HPC resources from CINES under allocation 2019-A0072B10315 attributed by GENCI (Grand Equipement National de Calcul Intensif) and from the "Mésocentre" computing center of CentraleSupélec and École Normale Supérieure Paris-Saclay (supported by CNRS and Région Île de France).

[1] A. K. Gupta, D. G. Lilley, N. Syred, Swirl Flows, Abacus Press, 1984.
[2] M. M. Ribeiro, J. H. Whitelaw, Coaxial jets with and without swirl, Journal of Fluid Mechanics 96 (4) (1980) 769–795.
[3] R.-H. Chen, J. F. Driscoll, The role of the recirculation vortex in improving fuel-air mixing within swirling flames, Symposium (International) on Combustion 22 (1) (1989) 531–540.
[4] S. H. Park, H. D. Shin, Measurements of entrainment characteristics of swirling jets, International Journal of Heat and Mass Transfer 36 (16) (1993) 4009–4018.
[5] R. Örlü, P. H. Alfredsson, An experimental study of the near-field mixing characteristics of a swirling jet, Flow, Turbulence and Combustion 80 (3) (2008) 323–350.
[6] F. Chang, V. K. Dhir, Mechanisms of heat transfer enhancement and slow decay of swirl in tubes using tangential injection, International Journal of Heat and Fluid Flow 16 (Issue 2) (1995) 78–87.
[7] W. Steenbergen, J. Voskamp, The rate of decay of swirl in turbulent pipe flow, Flow Measurement and Instrumentation 9 (2) (1998) 67–78.
[8] N. Syred, N. A. Chigier, J. M. Beér, Flame stabilization in recirculation zones of jets with swirl, Symposium (International) on Combustion 13 (1) (1971) 617–624.
[9] J. M. Beér, N. A. Chigier, Combustion aerodynamics, New York, 1972.
[10] N. Syred, J. M. Beér, Combustion in swirling flows: A review, Combustion and Flame 23 (2) (1974) 143–201.
[11] D. G. Lilley, Swirl flows in combustion: A review, AIAA Journal 15 (8) (1977) 1063–1078.
[12] R. Weber, J. Dugué, Combustion accelerated swirling flows in high confinements, Progress in Energy and Combustion Science 18 (4) (1992) 349–367.
[13] Y. Huang, V. Yang, Effect of swirl on combustion dynamics in a lean-premixed swirl-stabilized combustor, Proceedings of the Combustion Institute 30 II (2005) 1775–1782.
[14] Y. Huang, V. Yang, Dynamics and stability of lean-premixed swirl-stabilized combustion 35 (4) (2009) 293–364.
[15] N. S. A. Valera-Medina, P. Bowen, A. Crayford, Studies of swirl burner characteristics, flame lengths and relative pressure amplitudes, Journal of Fluids Engineering 133 (10) (2011) 101302.
[16] S. Candel, D. Durox, T. Schuller, J.-F. Bourgouin, J. P. Moeck, Dynamics of swirling flames, Annual Review of Fluid Mechanics 46 (2014) 147–173.

[17] C. O. Paschereit, E. Gutmark, W. Weisenstein, Excitation of thermoacoustic instabilities by interaction of acoustics and unstable swirling flow 38 (6) (2000) 1025–1034.
[18] A. M. Steinberg, I. Boxx, M. Stöhr, C. D. Carter, W. Meier, Flow–flame interactions causing acoustically coupled heat release fluctutations in a thermo-acoustically unstable gas turbine model combustor 157 (2010) 2250–2266.
[19] O. Lucca-Negro, T. O'Doherty, Vortex breakdown: a review, Progress in Energy and Combustion Science 27 (4) (2001) 431–481.
[20] R. E. Spall, T. B. Gatski, C. E. Grosch, A criterion for vortex breakdown., Physics of Fluids 30 (11) (1987) 3434–3440.
[21] P. Billant, J.-M. Chomaz, P. Huerre, Experimental study of vortex breakdown in swirling jets, Journal of Fluid Mechanics 376 (1998) 183–219.
[22] H. Liang, T. Maxworthy, An experimental investigation of swirling jets, Journal of Fluid Mechanics 525 (2005) 115–159.
[23] W. G. Rose, A swirling round turbulent jet, Journal of Applied Mechanics 29 (4) (1962) 615–625.
[24] N. A. Chigier, J. M. Beér, Velocity and static-pressure distributions in swirling air jets issuing from annular and divergent nozzles, Journal of Basic Engineering 86 (4) (1964) 788–796.
[25] N. A. Chigier, A. Chervinsky, Experimental investigation of swirling vortex motion in jets, Journal of Applied Mechanics 34 (2) (1967) 443–451.
[26] N. A. Chigier, A. Chervinsky, Aerodynamic study of turbulent burning free jets with swirl, Symposium (International) on Combustion 11 (1) (1967) 489–499.
[27] K. S. Yajnik, M. V. Subbaiah, Experiments on swirling turbulent flows. Part 1. Similarity in swirling flows, Journal of Fluid Mechanics 60 (4) (1973) 665–687.
[28] A. J. Reynolds, Similarity in swirling wakes and jets, Journal of Fluid Mechanics 14 (2) (1962) 241–243.
[29] J. K. Harvey, Some observations of the vortex breakdown phenomenon, Journal of Fluid Mechanics 14 (4) (1962) 585–592.
[30] K. Oberleithner, M. Sieber, C. N. Nayeri, C. O. Paschereit, C. Petz, H.-C. Hege, B. R. Noack, I. Wygnanski, Three-dimensional coherent structures in a swirling jet undergoing vortex breakdown: Stability analysis and empirical mode construction, Journal of Fluid Mechanics 679 (2011) 383–414.
[31] K. Manoharan, M. Frederick, S. Clees, J. O'Connor, S. Hemchandra, A weakly nonlinear analysis of the precessing vortex core oscillation in a variable swirl turbulent round jet, Journal of Fluid Mechanics 884 (2020) A29.
[32] T. Sarpkaya, On stationary and travelling vortex breakdowns, Journal of Fluid Mechanics 45 (3) (1971) 545–559.
[33] P. M. Anacleto, E. C. Fernandes, M. V. Heitor, S. I. Shtork, Swirl flow structure and flame characteristics in a model lean premixed combustor 175 (8) (2003) 1369–1388.
[34] N. Syred, A review of oscillation mechanisms and the role of the precessing vortex core (PVC) in swirl combustion systems 32 (2) (2006) 93–161.
[35] S. Roux, G. Lartigue, T. Poinsot, U. Meier, C. Bérat, Studies of mean and unsteady flow in a swirled combustor using experiments, acoustic analysis, and large eddy simulations 141 (2005) 40–54.
[36] K. Oberleithner, S. Terhaar, L. Rukes, C. O. Paschereit, Why non-uniform density suppresses the precessing vortex core, no. GT2013-95509, 2013.
[37] J. P. Moeck, J.-F. Bourgouin, D. Durox, T. Schuller, S. Candel, Nonlinear interaction between a precessing vortex core and acoustic oscillations in a turbulent swirling flame, Combustion and Flame 159 (8) (2012) 2650–2668.
[38] S. Farokhi, R. Tagavi, E. J. Rice, Effect of initial swirl distribution on the evolution of a turbulent jet, AIAA Journal 27 (6) (1989) 700–706.
[39] J. Panda, D. K. McLaughlin, Experiments on the instabilities of a swirling jet, Physics of Fluids 6 (1) (1994) 263–276.
[40] I. Toh, D. Honnery, J. Soria, Axial plus tangential entry swirling jet, Experiments in Fluids 48 (2) (2010) 309–325.
[41] R. T. Gilchrist, J. W. Naughton, Experimental study of incompressible jets with different initial swirl distributions: Mean results, AIAA Journal 43 (4) (2005) 741–751.
[42] M. P. Escudier, J. J. Keller, Recirculation in swirling flow: A manifestation of vortex breakdown, AIAA Journal 23 (1) (1985) 111–116.
[43] H. Altgeld, W. P. Jones, J. Wilhelmi, Velocity measurements in a confined swirl driven recirculating flow, Experiments in Fluids 1 (2) (1983) 73–78.
[44] G. Li, E. J. Gutmark, Effect of exhaust nozzle geometry on combustor flow field and combustion characteristics, Proceedings of the Combustion Institute 30 II (2005) 2893–2901.
[45] S. Terhaar, B. C. Bobusch, C. O. Paschereit, Effects of outlet boundary conditions on the reacting flow field in a swirl-stabilized burner at dry and humid conditions, Journal of Engineering for Gas Turbines and Power 134 (2012) 111501.
[46] S. B. Pope, Turbulent Flows, Cambridge University Press, 2000.
[47] J. Mattingly, G. Oates, An experimental investigation of the mixing of coannular swirling flows, AIAA Journal 24 (5) (1986) 785–792.
[48] Y. Zhao, R. Weber, Corrigendum to "Combustion accelerated swirling flows in high confinements" (Progress in Energy and Combustion Science (1992) 18(4) (349367)), Progress in Energy and Combustion Science 78 (2020) 2019–2020.
[49] R.-H. Chen, J. F. Driscoll, J. Keller, M. Namazian, R. W. Schefer, A comparison of bluff-body and swirl-stabilized flames, Combustion Science and Technology 71 (4-6) (1990) 197–217.
[50] T. Claypole, N. Syred, The effect of swirl burner aerodynamics on NOx formation, Symposium (International) on Combustion 18 (1) (1981) 81–89.
[51] Y. Zhang, D. Shimokuri, Y. Mukae, S. Ishizuka, Flow field in swirl-type tubular flame burner, JSME International Journal Series B Fluids and Thermal Engineering 48 (4) (2005) 830–838.
[52] D. Durox, J. P. Moeck, J.-F. Bourgouin, P. Morenton, M. Viallon, T. Schuller, S. Candel, Flame dynamics of a variable swirl number system and instability control, Combustion and Flame 160 (9) (2013) 1729–1742.
[53] H. Sheen, W. Chen, S. Jeng, T. Huang, Correlation of swirl number for a radial-type swirl generator, Experimental Thermal and Fluid Science 12 (4) (1996) 444–451.
[54] J. Choi, E. Jung, S. Kang, H. Do, Modeling Swirl Decay Rate of Turbulent Flows in Annular Swirl Injectors, AIAA Journal 56 (12) (2018) 4910–4926.
[55] A. Degenève, P. Jourdaine, C. Mirat, J. Caudal, R. Vicquelin, T. Schuller, Effects of a Diverging Cup on Swirl Number, Flow Pattern, and Topology of Premixed Flames, Journal of Engineering for Gas Turbines and Power 141 (2019) 031022.

[56] J. Sislian, R. Cusworth, Measurements of mean velocity and turbulent intensities in a free isothermal swirling jet, AIAA Journal 24 (2) (1986) 303–309.
[57] T. Mahmud, J. S. Truelove, T. F. Wall, Flow Characteristics of Swirling Coaxial Jets From Divergent Nozzles, Journal of Fluids Engineering 109 (3) (1987) 275–282.
[58] D. Durox, K. Prieur, T. Schuller, S. Candel, Different Flame Patterns Linked With Swirling Injector Interactions in an Annular Combustor, Journal of Engineering for Gas Turbines and Power 138 (10) (2016) 101504.
[59] J.-F. Bourgouin, J. Moeck, D. Durox, T. Schuller, S. Candel, Sensitivity of swirling flows to small changes in the swirler geometry, Comptes Rendus Mécanique 341 (1-2) (2013) 211–219.
[60] S. Candel, D. Durox, T. Schuller, P. Palies, J.-F. Bourgouin, J. P. Moeck, Out of equilibrium dynamics progress and challenges in swirling flame dynamics, Comptes Rendus Mécanique 340 (2012) 758–768.
[61] P. Palies, D. Durox, T. Schuller, P. Morenton, S. Candel, Dynamics of premixed confined swirling flames, Comptes Rendus Mécanique 337 (6-7) (2009) 395–405.
[62] M. Philip, Dynamique de l'allumage circulaire dans les foyers annulaires multi-injecteurs, Ph.D. thesis, École Centrale Paris (2016).
[63] O. Colin, M. Rudgyard, Development of High-Order TaylorGalerkin Schemes for LES, Journal of Computational Physics 162 (2) (2000) 338–371.
[64] H. Baya Toda, O. Cabrit, G. Balarac, S. Bose, J. Lee, H. Choi A N, F. Nicoud, A subgrid-scale model based on singular values for LES in complex geometries, in: Proceedings of the Summer Program of the Center for Turbulence Research, 2010.
[65] T. Poinsot, S. Lele, Boundary conditions for direct simulations of compressible viscous flows, Journal of Computational Physics 101 (1) (1992) 104–129.
[66] F. Jaegle, O. Cabrit, S. Mendez, T. Poinsot, Implementation methods of wall functions in cell-vertex numerical solvers, Flow, Turbulence and Combustion 85 (2) (2010) 245–272.
[67] G. Daviller, M. Brebion, P. Xavier, G. Staffelbach, J.-D. Müller, T. Poinsot, A Mesh Adaptation Strategy to Predict Pressure Losses in LES of Swirled Flows, Flow, Turbulence and Combustion 99 (1) (2017) 93–118.
[68] F. Kreith, O. K. Sonju, The decay of a turbulent swirl in a pipe, Journal of Fluid Mechanics 22 (2) (1965) 257–271.
[69] C. J. Scott, K. W. Bartelt, Decaying annular swirl flow with inlet soild body rotation, Journal of Fluids Engineering, Transactions of the ASME 98 (1) (1976) 33–40.
[70] O. Kitoh, Experimental study of turbulent swirling flow in a straight pipe, Journal of Fluid Mechanics 225 (1991) 445–479.
[71] Y. Fu, J. Cai, S. M. Jeng, H. Mongia, Confinement effects on the swirling flow of a counter-rotating swirl cup, in: Proceedings of the 2005 ASME Turbo Expo, Reno-Tahoe, Nevada, USA, 2005.
[72] P. A. Dellenback, D. E. Metzger, P. G. Neitzel, Measurements in turbulent swirling flow through an abrupt axisymmetric expansion, AIAA Journal 26 (6) (1988) 669–681.
[73] L. Selle, Simulation aux grandes échelles des intéractions flamme / acoustique dans un écoulement vrillé, Ph.D. thesis, Institut National Polytechnique de Toulouse (2004).
[74] P. Palies, Dynamique et instabilités de combustion des flammes swirlées, Ph.D. thesis, École Centrale Paris (2010).
[75] I. E. Idel'chik, A. S. Ginevskiy, Handbook of hydraulic resistance, Begell House, 2007.

Appendix A Method to calculate the swirl number from CFD simulations

Based on the previous analysis it is possible to formulate a set of guidelines for the computation of the swirl number in incompressible isothermal flows. These guidelines are suggested to ensure a high level of generality and reproducibility, while keeping the process straightforward in practical systems. We here consider cases where the swirl number is determined from CFD simulations and we examine unconfined and confined situations.

The computation of the conventional swirl number S_{conv} (Eq. (30)) is quite straightforward and is discussed in section A.1. On the other hand, determining the more general swirl number S_P^f can be challenging and requires well converged statistics. If a compressible solver is used, the presence of even minute spurious pressure oscillations can greatly impact the computation of S_P^f. For this reason, the authors highly recommend examining the axial evolution of S_P^f in a manner similar to Fig. 16 to check for spurious oscillations in S_P^f. The method to determine S_P^f in an unconfined configuration is presented in section A.2 before the confined case is discussed in section A.3.

A.1 Determination of the conventional swirl number S_{conv}

The determination of the conventional swirl number S_{conv} is quite straightforward. Mean velocity profiles should be acquired at an axial section located as close to the outlet of the injector as possible and can be integrated as follow:

$$S_{conv} = \frac{\int_0^{R_{lim}} \rho \, \overline{U_\theta} \, \overline{U_x} \, r^2 dr}{R_{inj} \int_0^{R_{lim}} \rho \, \overline{U_x}^2 \, r dr} \qquad (30 \textit{ rep.})$$

The radial integration limit R_{lim} may be determined by plotting S_{conv} for different integration radii as shown in Fig. 17. When quoting a value of S_{conv}, the axial section at which it is determined and the integration limit R_{lim} should be specified so that the computation is reproducible.

A.2 Determination of S_P^f in an unconfined configuration

The calculation may proceed according to the following steps:

(1) Choose a reference radius R_{ref}. It is suggested to choose the radius of the outlet port of the injection system.

(2) Determine the far-field pressure p_∞:

- In the case of quiescent surroundings, this corresponds to the mean static pressure at infinity $p_\infty = \overline{p}(r = \infty)$.
- If a low velocity co-flow is present, $p_\infty = \overline{p}(r = \infty) + \rho(r = \infty)\overline{U_x}^2(r = \infty)$.

(3) Choose a practical integration limit R_{lim}. This should be inside the region where the numerical grid is sufficiently fine to allow an accurate calculation. It is recommended to verify this choice by plotting curves similar to those of Fig. 15 to check that the most of the flowrate of momentum is accounted for[3].

(4) Compute $G_{x,P}^f$, G_θ and finally S_P^f as

$$G_{x,P}^f = 2\pi \int_0^{R_{lim}} \left[\rho\left(\overline{U_x}^2 + \overline{u_x^2}\right) + (\overline{p} - p_\infty)\right] r dr \tag{A.1}$$

$$G_\theta^f = 2\pi \int_0^{R_{lim}} \rho\left(\overline{U_\theta}\,\overline{U_x} + \overline{u_\theta u_x}\right) r^2 dr \tag{A.2}$$

$$S_P^f = \frac{G_\theta^f}{R_{ref} G_{x,P}^f} \tag{A.3}$$

(5) It is recommended to calculate these terms at several axial positions downstream of the outlet port. They should be conserved.

A.3 Determination of S_P^f in a confined configuration

The procedure in this case may be as follows:

(1) Choose a reference radius R_{ref}. It is suggested to use the radius of the confinement[4].

(2) Choose a reference pressure p_{ref}. As in section 5.2, it is proposed to choose the sectional average of the static pressure at an axial position where the flow is established. This value may be determined by plotting the axial evolution of the sectional average of the static pressure.

(3) Compute $G_{x,P}^f$, G_θ^f by integration over the whole cross-section Σ and determine S_P^f as

$$G_{x,P}^f = \int_\Sigma \left[\rho\left(\overline{U_x}^2 + \overline{u_x^2}\right) + \left(\overline{p} - p_{ref}\right)\right] dS \tag{A.4}$$

$$G_\theta^f = \int_\Sigma \rho\left(\overline{U_\theta}\,\overline{U_x} + \overline{u_\theta u_x}\right) r\, dS \tag{A.5}$$

$$S_P^f = \frac{G_\theta^f}{R_{ref} G_{x,P}^f} \tag{A.6}$$

(4) It is recommended to calculate these terms at several axial positions. Only a slow decay along the axis corresponding to the skin friction on the wall of the channel should be observed[5].

[3] See footnote 6 on page 34.

[4] A hydraulic radius can be used for non-cylindrical confinements.

[5] See Appendix **??** for a discussion on the extension of the conservation properties of the swirl number for non-cylindrical confinements.

Appendix B Method to calculate the swirl number from experimental data

We consider in the present appendix cases where the swirl number is determined from experiments and we examine unconfined and confined situations. The computation of the conventional swirl number S_{conv} (Eq. (30)) is quite straightforward and the reader is referred to appendix A.1 for more details. The direct determination of the more general swirl number S_P^f may only be accomplished using intrusive Pitot tubes. The formulation S_U^f (Eqs. (29) and (44)) is better suited and provides a good estimate of S_P^f. In unconfined swirling jets, recommended practices for computing S_U^f are presented in section B.1. In section B.2, we discuss the challenges associated with the determination of S_U^f in confined configurations, and suggest two methods that may be used if the experimental challenges are overcome.

B.1 Determination of the swirl number S_U^f in unconfined flows

It is assumed that measurements are obtained from laser velocimetry techniques such as Laser Doppler Velocimetry (LDV) or Particle Image Velocimetry (PIV) and that the following time averaged quantities are available: axial velocity $\overline{U_x}$ and its axial gradient; axial velocity fluctuations $\overline{u_x}$; tangential velocity $\overline{U_\theta}$; tangential velocity fluctuations $\overline{u_\theta}$; radial velocity $\overline{U_r}$ and its axial gradient; radial velocity fluctuations $\overline{u_r}$; Reynolds stress term $\overline{u_x u_\theta}$; Reynolds stress term $\overline{u_x u_r}$ and its axial gradient. Given these requirements, the preferred measurement techniques are 2-component LDV, or 3-component stereo-PIV, which give access to both Reynold stress terms $\overline{u_x u_\theta}$ and $\overline{u_x u_r}$. The swirl number may then be determined with the following steps.

(1) Choose a reference radius R_{ref}. A natural choice is the radius of the outlet port of the injection system.

(2) Choose a practical integration limit R_{lim}. The integration should be stopped where the axial velocity and its fluctuations are close to zero (or u_∞ if applicable)[6].

(3) S_U^f can now be computed as per Eq. (29). First, compute G_θ^f as

$$G_\theta^f = 2\pi \int_0^{R_{lim}} \rho \left(\overline{U_\theta}\,\overline{U_x} + \overline{u_\theta u_x}\right) r^2 dr \tag{B.1}$$

(4) Compute $G_{x,U}^f$ as

$$G_{x,U}^f = 2\pi \int_0^{R_{lim}} \rho \left[\overline{U_x}^2 + \overline{u_x^2} - \frac{1}{2}\left(\overline{U_\theta}^2 + \overline{U_r}^2 + \overline{u_r^2} + \overline{u_\theta^2}\right) + \frac{r}{2}\frac{\partial}{\partial x}\left(\overline{U_x}\,\overline{U_r} + \overline{u_x u_r}\right)\right] r dr \tag{B.2}$$

(5) Compute S_U^f as

$$S_U^f = \frac{G_\theta^f}{R_{ref} G_{x,u}^f} \tag{B.3}$$

(6) It is recommended to compute these terms at several axial positions downstream of the outlet port in order to validate the calculation by checking their conservation.

---

[6] In practice, a good point to start is $R_{lim} \geq 2R_{ref}$. If R_{lim} is sufficiently large, G_θ^f and $G_{x,U}^f$ are independent of R_{lim}. Thus, consider plotting graphs similar to Fig. 20, check for the following properties and increase R_{lim} until they are satisfied:

(a) All velocities and the static pressure at this position should be close to their value at $r = \infty$

(b) $2\pi R_{ref} R_{lim} \left[\rho\left(\overline{U_x}^2(x, R_{lim}) + \overline{u_x^2}(x, R_{lim})\right) + \left(\overline{p}(x, R_{lim}) - p_\infty\right)\right] \ll G_{x,P}^f(x, R_{lim})$

(c) $2\pi R_{ref} R_{lim}^2 \rho\left(\overline{U_\theta}(x, R_{lim})\,\overline{U_x}(x, R_{lim}) + \overline{u_\theta u_x}(x, R_{lim})\right) \ll G_\theta^f(x, R_{lim})$

B.2 Determination of the swirl number S_U^f in confined flows

The determination of the swirl number S_U^f in confined flows presents two major challenges.

- As shown in section 5.5, the integration of the velocity profiles must be conducted up to the wall, the radial position closest to the wall conveying a large weight in the final results. This implies that all velocities, including cross-correlations such as $\overline{u_x u_\theta}$ or the axial gradient of $\overline{u_x u_r}$ must be accurately measured near the wall with a sufficiently high resolution. Although possible in some configurations using current laser velocimetry apparatus, it remains an arduous task.
- A reference pressure needs to be determined.

Given these difficulties, numerical simulations should be considered as a practical alternative if S_P^f or S_U^f are required. We nonetheless present here two methods to determine S_U^f in confined configurations: in the simpler, but more approximate, high Reynolds number method of section B.2.1, all viscous losses are neglected. Measurements are conducted at an axial section where the flow is established, thereby removing the need for the determination of the reference pressure. A more complex method which does not involve any simplifying assumptions is given in section B.2.2.

B.2.1 Simple method: high Reynolds number approach

The method presented in this section applies to confined swirling jets in configuration with a constant cross-section Σ. It is demonstrated in section 2, and verified in section 5.1 that, if viscous dissipation is negligible, the swirl number is conserved in a cylindrical duct. Similar conservation properties are demonstrated in the case of non-cylindrical confinements with constant cross-section in appendix **??**. It is then natural to attempt to measure the swirl number at an axial section where the flow is established, and where many complexities related to the radial expansion of the flow can be neglected. In particular, with the definition of the reference pressure put forward in section 5.2, it becomes unnecessary to determine either the static pressure or the reference pressure: $\int_\Sigma \left(\overline{p} - p_{ref}\right) dS = 0$.

The swirl number may then be determined with the following steps.

(1) Choose a reference radius R_{ref}. It is suggested to use the radius of the confinement[7].

(2) Compute G_θ^f by integration over the entire cross-section as [8]

$$G_\theta^f = \int_\Sigma \rho \left(\overline{U_\theta}\,\overline{U_x} + \overline{u_\theta u_x}\right) r dS \tag{B.5}$$

(3) Compute $G_{x,U}^f$. The following formula only applies in axial sections where the flow is established[9].

$$G_{x,U}^f = \int_\Sigma \rho \left[\overline{U_x}^2 + \overline{u_x^2}\right] dS \tag{B.7}$$

(4) Compute S_u^f as

$$S_U^f = \frac{G_\theta^f}{R_{ref} G_{x,U}^f} \tag{B.8}$$

[7] A hydraulic radius can be used for non-cylindrical confinements.

[8] Alternatively, for a confinement with a cylindrical cross-section:

$$G_\theta^f = 2\pi \int_0^{R_c} \rho \left(\overline{U_\theta}\,\overline{U_x} + \overline{u_\theta u_x}\right) r^2 dr \tag{B.4}$$

[9] Alternatively, for a confinement with a cylindrical cross-section:

$$G_{x,U}^f = 2\pi \int_0^{R_c} \rho \left[\overline{U_x}^2 + \overline{u_x^2}\right] r dr \tag{B.6}$$

(5) It is recommended to compute these terms at several axial positions where the flow is established in order to validate the calculation by checking the conservation of G_θ^f, $G_{x,U}^f$ and S_U^f.

B.2.2 Complex method: injector near-field measurements

This method requires the velocity field to be measured in at least two axial section thereafter referred to as Σ_1 and Σ_2. The flow must be established at Σ_1, which serves to determine the reference pressure. Σ_2 may be found in the vicinity of the injection unit or wherever the experimenter sees fit. It is assumed here that the cross-section does not vary: $\Sigma_1 = \Sigma_2$. The difference in wall pressure between these two axial sections $\Delta P_{21} = \overline{p}(r = R_c, x = x_{\Sigma 2}) - \overline{p}(r = R_c, x = x_{\Sigma 1})$ must also be measured using a sensitive differential pressure gauge.

All steps presented in the previous section B.2.1 may be applied to the velocity field measured at section Σ_2 with the exception of step (3) where the following formula must be employed

$$\begin{aligned} G_{x,U}^f(\Sigma_2) = &\int_{\Sigma_2} \rho \left[\overline{U_x}^2 + \overline{u_x^2} - \frac{1}{2}\left(\overline{U_\theta}^2 + \overline{U_r}^2 + \overline{u_r^2} + \overline{u_\theta^2} \right) + \frac{r}{2}\frac{\partial}{\partial x}\left(\overline{U_x}\,\overline{U_r} + \overline{u_x u_r} \right) \right]_{\Sigma_2} dS \\ &+ \Sigma_2 \Delta P_{21} - \int_{\Sigma_1} \rho \left[-\frac{1}{2}\left(\overline{U_\theta}^2 + \overline{U_r}^2 + \overline{u_r^2} + \overline{u_\theta^2} \right) + \frac{r}{2}\frac{\partial}{\partial x}\left(\overline{U_x}\,\overline{U_r} + \overline{u_x u_r} \right) \right]_{\Sigma_1} dS \end{aligned} \tag{B.9}$$

Alternatively to the use of Eq. (B.9), in a configuration similar to that used in the present study (depicted schematically in Fig. 22, where the outlet of a simple cylindrical combustor is found in a quiescent atmosphere, the use of analytical jump conditions such as those presented in Appendix D (Eqs. (D.3) or (D.6)) may be considered to determine a reference pressure and subsequently compute the swirl number using Eq. (44).

Appendix C Can swirl numbers measured in a free swirling jet be extended to a confined configuration ?

In order to test the proposed swirl number computation method on a free swirling jet, it is here applied to the same injector and operating conditions, but without the quartz confinement tube. The values of S_U^f and S_{conv} for the free swirling jet are then compared to their counterpart for the confined flow. We thus examine whether swirl number measured in unconfined cases (which are generally far easier to investigate in terms of measurement apparatus) may easily be extended to a confined configuration.

To this end, LDV measurements are performed at $x = 5, 10$ and $20\,\mathrm{mm}$. As per the LDV system specifications and accounting for statistical uncertainties (assuming an underlying gaussian distribution), measurement uncertainties are under $0.25\,\mathrm{m\,s^{-1}}$ for both mean and RMS velocities. The relative measurement uncertainty for cross-correlation are better than 40% for $r < 15\,\mathrm{mm}$, but can reach up to 100% for $r > 15\,\mathrm{mm}$. Imperfections in the seeding are not accounted for. Results are presented in Fig. 18 and 19, and compared with the confined velocity profiles from the LES, which have been previously thoroughly validated in Fig. 4. In the outer regions, as could be expected, the flow differs significantly between the two configurations, and in particular, the unconfined case does not have an outer recirculation zone. The unconfined jet is also much narrower than its confined counterpart, with a weaker and narrower inner recirculation zone. The unconfined jet is not spreading as widely, and the maximum axial velocity is found to remain around $r \approx 6\,\mathrm{mm}$ at $z = 5, 10$ and $20\,\mathrm{mm}$.

Let us now compute the swirl number S_U^f (Eq. 29) as recommended per the procedure of appendix B.1. In the present case, the reference radius is naturally the radius of the injector $R_{ref} = R_{inj} = 5\,\mathrm{mm}$. The choice of the limit R_{lim} for the integration is based on the analysis presented in Fig. 20. It shows the impact of R_{lim} on $G_{x,U}^f$ and G_θ^f, whose formulas are repeated below for a free swirling jet

$$G_{x,U}^f = 2\pi \int_0^{R_{lim}} \rho \left[\overline{U_x}^2 + \overline{u_x^2} - \frac{1}{2}\left(\overline{U_\theta}^2 + \overline{U_r}^2 + \overline{u_r^2} + \overline{u_\theta^2} \right) + \frac{r}{2}\frac{\partial}{\partial x}\left(\overline{U_x}\,\overline{U_r} + \overline{u_x u_r} \right) \right] r dr \tag{C.1}$$

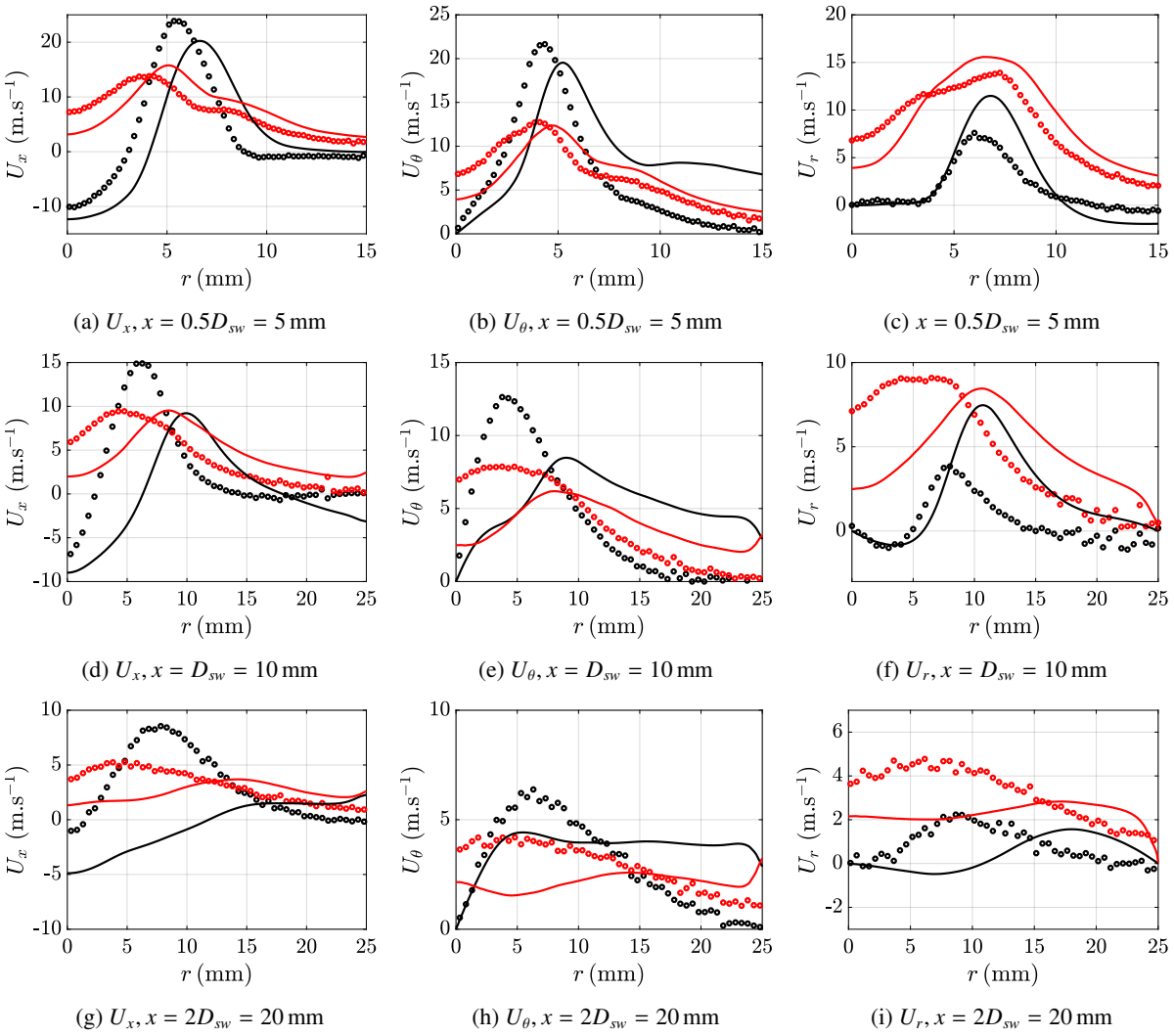

(a) U_x, $x = 0.5D_{sw} = 5$ mm (b) U_θ, $x = 0.5D_{sw} = 5$ mm (c) $x = 0.5D_{sw} = 5$ mm

(d) U_x, $x = D_{sw} = 10$ mm (e) U_θ, $x = D_{sw} = 10$ mm (f) U_r, $x = D_{sw} = 10$ mm

(g) U_x, $x = 2D_{sw} = 20$ mm (h) U_θ, $x = 2D_{sw} = 20$ mm (i) U_r, $x = 2D_{sw} = 20$ mm

Figure 18: Time averaged velocity profiles obtained using LES in the confined case (continuous lines, confinement with a 25 mm radius) and measured with LDV in the unconfined case (symbols). Both mean (in black) and RMS (in red) values are shown at three distances from the combustor backplane. From left to right: axial, tangential and radial velocity profiles.

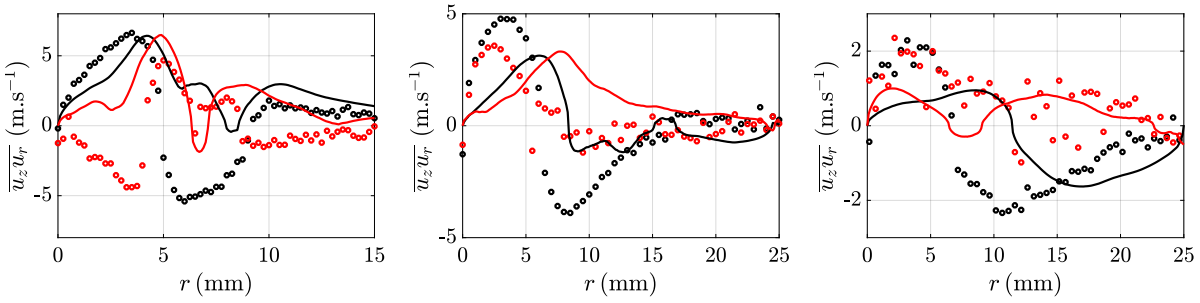

(a) $x = 0.5D_{sw} = 5$ mm (b) $x = D_{sw} = 10$ mm (c) $x = 2D_{sw} = 20$ mm

Figure 19: Time averaged velocity cross-correlation profiles obtained using LES in the confined case (continuous lines, confinement with a 25 mm radius) and measured with LDV in the unconfined case (symbols). Both $\overline{u_z u_r}$ (in black) and $\overline{u_z u_\theta}$ (in red) values are shown at three distances from the combustor backplane.

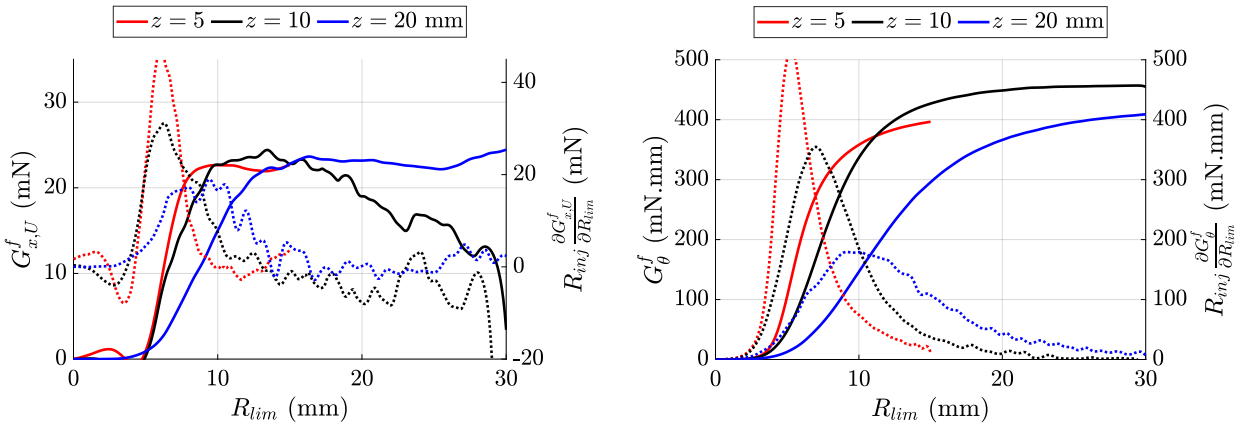

(a) $G^f_{x,P}$ (b) G^f_θ

Figure 20: Effect of integration limit on the estimated flow rates $G^f_{x,U}$ (left, plain line) and G^f_θ (right, plain line) at $z = 5$, 10 and 20 mm. The integral terms are computed by stopping the integration at various distances R_{lim}. As recommended in appendix B, the derivative with regards to R_{lim} of the momentum flowrates are shown as dotted lines. They are multiplied by the radius of the injector R_{inj} for scaling.

$$G^f_\theta = 2\pi \int_0^{R_{lim}} \rho \left(\overline{U_\theta}\,\overline{U_x} + \overline{u_\theta u_x}\right) r^2 dr \tag{C.2}$$

The derivative of these terms with respect to R_{lim} is scaled by R_{inj} and shown alongside (dotted lines in Fig. 20). Let us first consider $z = 10$ mm (black curves). From Fig. 18, the axial velocity is close to zero after $r = 15$ mm: $\overline{U_x}(z = 10, r > 15) \approx 0$. Figure 20(b) shows that, for $R_{lim} > 15$ mm, G^f_θ is nearly constant and $R_{inj}\,\partial G^f_\theta/\partial R_{lim}$ is small. Figure 20(a) shows that $G^f_{x,U}(R_{lim})$ is constant around $R_{lim} = 15$ mm. We also observe that $R_{inj}\,\partial G^f_{x,U}/\partial R_{lim} \approx 0$ at $R_{lim} = 15$ mm. However, $G^f_{x,U}(R_{lim})$ gets smaller for larger values of R_{lim}. Given the estimated measurement uncertainties, it appears reasonable to attribute the decay of $G^f_{x,U}$ for $R_{lim} > 15$ mm to measurement noise. One may then chose $R_{lim}(z = 10\,\text{mm}) = 15$ mm. The values of R_{lim} at the two other axial sections are chosen using the same process: $R_{lim}(z = 5\,\text{mm}) = 15$ mm and $R_{lim}(z = 20\,\text{mm}) = 25$ mm. From Fig. 20, one also observes that the values of $G^f_{x,U}$ and G^f_θ are fairly constant between the three axial positions $z = 5$, 10 and 20 mm as is expected for a free swirling jet.

Concerning the conventional swirl number S_{conv}, we retain for both the confined flow and the free jet the same integration limit of $2R_{inj}$ (section 6):

$$S_{conv} = \frac{\int_0^{2R_{inj}} \rho\,\overline{U_\theta}\,\overline{U_x}\,r^2 dr}{R_{inj}\int_0^{2R_{inj}} \rho\,\overline{U_x}^2\,r dr} \tag{C.3}$$

In Fig. 21, swirl numbers obtained in the confined case (black) using Eqs. (40) (S^f_P), (44) (S^f_U) and (42) (S_{conv}) are compared with swirl numbers computed in the unconfined case (red, LDV). The swirl number for the free jet, computed using Eq. (29) (S^f_U) are tightly grouped together as is expected from the conservation properties. However, the conventional swirl number S_{conv} (Eq. (30)) has a much higher variability. While the values of S_{conv} are reasonably similar between the confined and unconfined cases at $x = 2.5$ and 5 mm, S^f_U differs significantly. This could be expected because the mean velocity profiles are quite similar close to the outlet of the injector, but become quite different further downstream. This large effect of the confinement is coherent with the literature on swirling flow showing examples of such confinement induced changes in near-injector flowfields [42, 43, 71].

From this, one can conclude that swirl numbers (S^f_P and S^f_U) of confined flows may not be directly compared to swirl numbers (S^f_P and S^f_U) measured in unconfined jets. On the other hand, in the present configuration, the values of the conventional swirl number S_{conv} are reasonably close provided that they are evaluated close to the outlet of the injector.

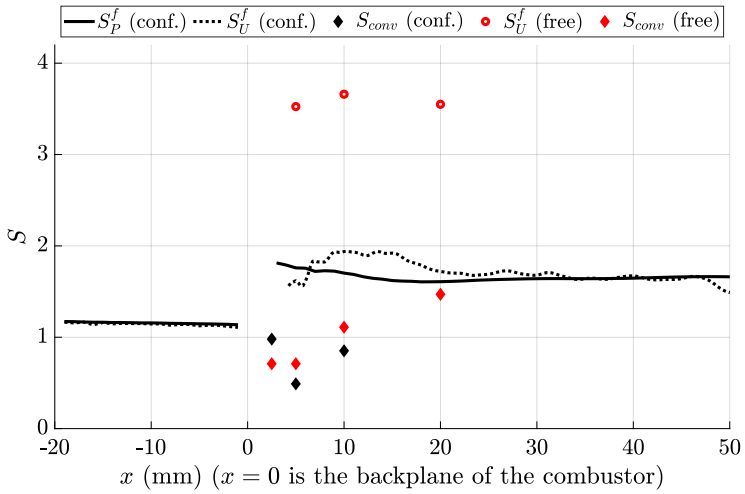

Figure 21: Comparison of different swirl numbers computed in the confined case (LES, black) and in the free jet (red, LDV).

Appendix D A jump condition to determine the reference pressure

It is worth examining the jumps in $G^f_{x,P}$ and G^f_θ at the sudden expansion. In the present appendix, these jumps are used to derive a method for determining the jump in reference pressure, which may be used as an alternative to Eq. (B.9). The fate of swirling flows after an area change is investigated, for example, in [72], with detailed experimental determination of velocity profiles, and correlations for vortex breakdown regimes and precessing vortex core frequency. This configuration is also studied in the vortex breakdown literature [19–22], the usual configuration being a swirl flow at a sudden expansion, but in water at a lower upstream Reynolds number. However, the evolution of the swirl number itself is not often considered. This matter is briefly discussed in [73] and in [74], and there is also a recent study of the effect of a conical cup fitted to a cylindrical injector in [55]. Choi et al. [54] propose a 1D low-order model for the swirl number evolution in injectors featuring an annular cross-section with expansion and contraction. However, the pressure term is not accounted for in the swirl number formulation.

Figure 10 shows the sizable changes in $G^f_{x,P}$ and S^f_P at the sudden expansion, while G^f_θ only features a relatively small jump. From a straightforward application of momentum balance to the control volume defined in Fig. 22, combined with assumptions that the flow is incompressible and isothermal, and that viscous effects can be neglected, one may write jump relations between the upstream (−) and downstream (+) sections:

$$G^f_\theta\Big|_+ = G^f_\theta\Big|_- \tag{D.1}$$

$$G^f_{x,P}\Big|_+ - G^f_{x,P}\Big|_- = 2\pi \int_{R_-}^{R_+} r\ \overline{p}|_{x=0}\ dr - \left[\Sigma|_+\, p_{ref}(+) - \Sigma|_-\, p_{ref}(-)\right] \tag{D.2}$$

where the right hand term accounts for the pressure force on the backplane and the change in reference pressure. $\Sigma|_+$ and $\Sigma|_-$ designate the downstream and upstream cross-sectional areas respectively. The change in the axial flux of axial momentum can thus be decomposed in two contributions: the change in reference pressure and the force exerted on the backplane. The latter is linked to the singular head loss at the sudden expansion. The change in reference pressure may be derived from the jump condition of $G^f_{x,P}$, and this process is described in what follows.

In compliance with property [P2] (section 5.2), two reference pressures are defined, corresponding to the upstream (−) and downstream (+) sections. Without any simplifying assumption, the change in reference pressure is linked to the singular head loss ΔP_{loc} at the sudden expansion by

$$p_{ref}(-) - p_{ref}(+) = \Delta P_{loc} - \frac{1}{2}\frac{\dot{m}^2}{\rho}\left(\frac{\mathrm{M}|_-}{\Sigma|_-^2} - \frac{\mathrm{M}|_+}{\Sigma|_+^2}\right) \tag{D.3}$$

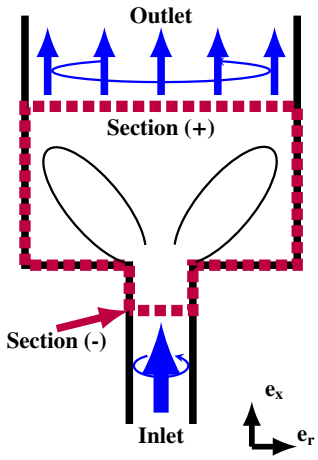

Figure 22: Schematic illustration of the control volumes used in Eq. (D.1) and (D.2). Sections (-) and (+) are located on the upstream and downstream side of the sudden expansion; the swirling jet and its expansion is represented by two black elliptic lines.

The flow momentum coefficient M (Boussinesq coefficient) is defined in [75]

$$\mathrm{M} = \frac{\pi {R_c}^2 \int_0^{R_c} \left[\overline{U_x}^2 + \overline{u_x^2}\right] r dr}{\left(\int_0^{R_c} \overline{U_x} r dr\right)^2} \tag{D.4}$$

and used to estimate the singular head loss coefficient ξ_{loc} under the assumption that $\mathrm{M}|_-$ is close to unity

$$\xi_{loc} = \frac{2\rho\, \Sigma|_-^2}{\dot{m}^2} \Delta P_{loc} \simeq (3\ \mathrm{M}|_- - 2)\left[1 - \frac{2\ \Sigma|_-}{3\ \Sigma|_+}\right] + \frac{\Sigma|_-^2}{\Sigma|_+^2} - \frac{4\ \Sigma|_-}{3\ \Sigma|_+} \tag{D.5}$$

Using these relationships a jump condition for the reference pressure is obtained based only on the upstream Boussinesq coefficient $\mathrm{M}|_-$ and well-known geometric and operational parameters. Figure 23 shows that in the present case, the Boussinesq coefficient M, section averaged total $\langle \overline{p}_{tot} \rangle$ and static $\langle \overline{p} \rangle$ pressures can be considered to be constant where the flow is established. This is coherent with previous experimental measurements in [69, 70] where the shape of the velocity profiles is found to be conserved.

In the present case, the simulation yields $\Delta P_{loc} = 317\,\mathrm{Pa}$, and the Boussinesq coefficients $\mathrm{M}|_- = 1.3$ and $\mathrm{M}|_+ = 3.2$. The estimate for ΔP_{loc} from Eq. (D.5) is 318 Pa. In section 5.2, the reference pressures were chosen as $p_{ref}(+) = 101\,325.3\,\mathrm{Pa}$ in the downstream duct and $p_{ref}(-) = 101\,405\,\mathrm{Pa}$ in the cylindrical injector, which gives $p_{ref}(-) - p_{ref}(+) = 80\,\mathrm{Pa}$. Equation (D.3) yields $p_{ref}(-) - p_{ref}(+) = 88\,\mathrm{Pa}$.

In practive, Eq. (D.3) may be used to estimate the reference pressure. For example, for a ducted swirling flow exhausting to a quiescent atmosphere, the reference pressure in the duct may be readily estimated by recasting Eq. (D.3) and (D.5):

$$p_{ref} \simeq p_{atm} + \frac{\dot{m}^2}{\rho \Sigma^2} [\mathrm{M} - 1] \tag{D.6}$$

where M is the Boussinesq coefficient computed at an axial section where the flow is established in the duct.

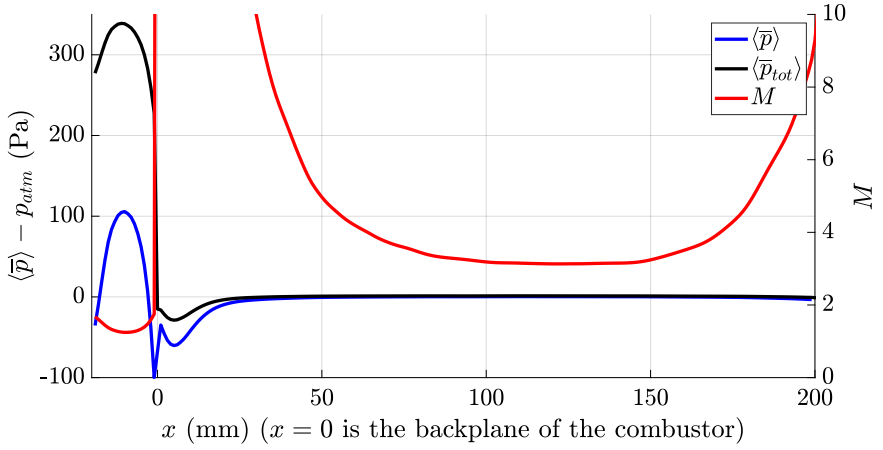

Figure 23: Axial evolution of the section averaged static (blue) and total (black) pressure $\langle\overline{p}_{tot}\rangle = \langle\overline{p} + 1/2\rho\left(\overline{U}^2 + \overline{u^2}\right)\rangle$ in the system (left axis). The atmospheric pressure $p_{atm} = 101\,325$ Pa is removed. Values of the Boussinesq momentum coefficient M (red) are given in the right axis.